ALMA MATER STUDIORUM – UNIVERSITÀ DI BOLOGNA

SCHOOL OF SCIENCE
Department of Physics and Astronomy
Master Degree Programme in Astrophysics and Cosmology

High-resolution chemical makeup of the disrupted metal-poor stellar cluster ED-2

Graduation Thesis

Presented by:
Sara Covella

Supervisor:
Prof. Alessio Mucciarelli
Dr. Edoardo Ceccarelli

Academic year 2024-2025

Graduation date III

Contents

Chapter 1

Introduction

This research is framed within the context of *Galactic Archaeology*, which aims to reconstruct the formation and evolution of the Milky Way and its stellar populations by studying its oldest constituents. The fundamental idea at the basis of this field is to use the properties of long-lived stars to reconstruct the history of our Galaxy.

The Milky Way (MW) is a disk galaxy characterised by different components, namely the bulge, the thin and thick disk and the stellar halo, which are shown in Fig.1.1. The basic assumption in the description of galactic evolution concerns the adopted cosmological paradigm, which is the Λ Cold Dark Matter model (ΛCDM). According to this, galaxies grow their masses through hierarchical merging, which means that smaller galaxies progressively merge in order to form larger and more complex systems. Specifically, when small galaxies are accreted onto a massive progenitor, their debris contributes to the formation of the host halo. This is the reason why the galactic component that bears the most information to reconstruct the Milky Way's evolution is the stellar halo.

More in detail, the dynamics of halo stars is one of the most powerful tools to reconstruct the ancient history of the Milky Way. Initially, the stars belonging to the accreted system remain spatially and kinematically coherent in the form of a stream. Then, since the accreted system is torn apart by tidal forces, these stars phase-mix over time on a timescale that depends both on the orbit and on the internal properties of the system. The *phase mixing* effect hence implies that these stars lose their spatial coherence with time. However, even after the spatial coherence is completely lost, the coherence in the Integrals of Motion (IoM hereafter) space is maintained. This means that the dynamical analysis and in particular the search for substructures in the IoM space can be used to identify past merger events, whose debris is completely mixed-up in the plane of the sky.

The integrals of motion, such as energy, vertical angular momentum and actions, are conserved properties both along the orbit and with time at the first order (Helmi and de Zeeuw, 2000). In order to estimate the stars' integrals of motion, the six parameters of the phase space are needed and these are given by the three components of the position vector and by the three components of the velocity vector. From an observational point of view, the three components of the position vector are right ascension (RA), declination angle (DEC) and the distance, which can be computed as the inverse of the parallax. On the other hand, two out of the three components of the velocity vector are provided by the proper motion of stars while the third component is the velocity along the line of sight (LOS). Proper motions have historically been the most difficult to measure, because they are an angular quantity, and as such their

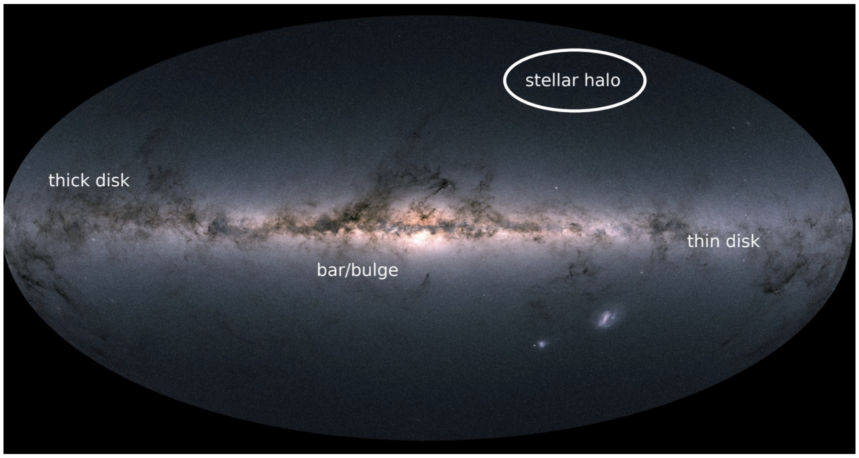

Figure 1.1: The four main components of the Milky Way are here represented: bar/bulge, thin disk, thick disk and stellar halo.

magnitude decreases linearly with distance. Thanks to the *Gaia* mission (Brown et al., 2018), though, proper motions have now been measured for more than 2 billion stars in the Milky Way. LOS velocities, instead, are measured spectroscopically from the Doppler effect of individual spectral lines.

The combination of the second data release of *Gaia* (*Gaia* DR2) with the data available from large spectroscopic surveys such as APOGEE (Apache Point Observatory Galactic Evolution Experiment, see Majewski et al., 2017), GALAH (Galactic Archaeology with HERMES, see Zwitter et al., 2018) and LAMOST (Large Sky Area Multi-Object Fibre Spectroscopic Telescope, see A L. Luo et al., 2015) has allowed to reconstruct the orbital properties, and thus the IoM, for many millions of stars. Such an unprecedented availability of dynamical information has provided a much clearer view of the early Milky Way evolution.

1.1 Current picture of the Milky Way assembly history

1.1.1 Gaia Enceladus

Among the most important discoveries carried out with the second data release of *Gaia* is the merging event with the Gaia-Sausage-Enceladus (GSE) dwarf galaxy (Helmi et al., 2018, Belokurov et al., 2018). In order to discover such merging event, the starting point is provided by the dynamics of halo stars in the solar neighbourhood. These nearby halo stars, that have highly precise parallax measurements, have been selected kinematically by excluding stars that move on disc-like circular orbits (see the blue-shaded area in Fig.1.2).

Looking at the distribution of halo stars in the IoM space, some clear properties can be appreciated. The first is that despite the exclusion of disc stars, a prominent population of sources exists with orbital properties similar to those of the disc. Secondly, it is possible to highlight the presence of some coherent clumps, which is suggestive of a common origin for their stars. Finally, and most importantly, a large clump of stars with slightly retrograde orbit ($L_z \lesssim 0$ km/s kpc) manifests as the most dominant feature.

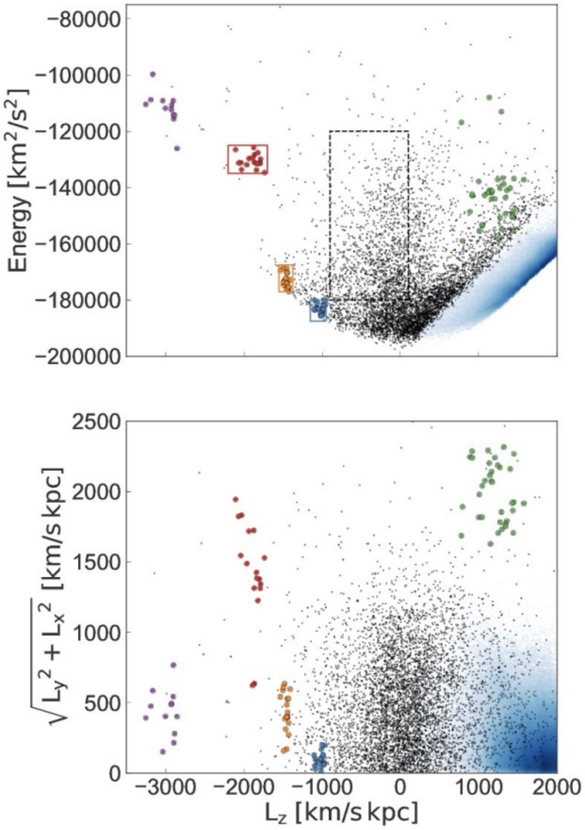

Figure 1.2: In the *top panel* the energy E is plotted as a function of the vertical angular momentum L_z for halo stars in the solar neighbourhood, while in the *bottom panel* the $L_\perp = \sqrt{L_x^2 + L_y^2}$ is plotted as a function of the vertical angular momentum once again for halo stars in the solar neighbourhood (e.g. H. Koppelman et al., 2018).

This is highlighted in the black rectangle of Fig.1.2. The presence of these dynamical over-densities suggests the existence of at least one merging event during the history of the Milky Way.

Still, for well-mixed debris, dynamics alone may be inconclusive, as one event can generate multiple IoM clumps or overlap with unrelated debris (Belokurov and Kravtsov, 2022). Therefore, chemical tagging is essential to disentangle the Milky Way's assembly history. In particular, in the $[\alpha/Fe]$ vs $[Fe/H]$ plot (see Fig.1.3) it is possible to notice that the clump of stars identified by the rectangular region is characterised by a knee that is positioned at lower metallicity with respect to the one for stars formed in situ (Matteucci and Romano, 1999). Knowing that the metallicity of the knee point gives informations about the star formation rate (SFR) of the environment in which these stars were formed, this means that all the stars belonging to the aforementioned dynamical blob were formed in an environment characterised by a low SFR, like a dwarf galaxy. This is the demonstration that those stars formed in the same dwarf galaxy progenitor called Gaia Enceladus.
Instead, halo stars moving on orbits similar to those of the disc show a knee point in the [α/Fe] vs [Fe/H] space at high metallicity. As such, they were likely in-situ stars that were dynamically heated to higher

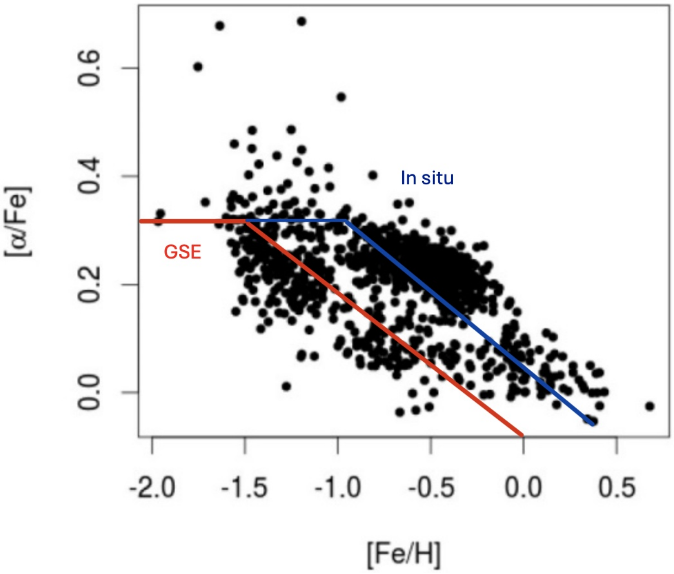

Figure 1.3: The $[\alpha/Fe]$ vs $[Fe/H]$ diagram for halo stars in the solar neighbourhood where it is possible to recognise two different sequences: one at lower and the other at higher metallicities (e.g. Gaia Collaboration Brown et al., 2018, Helmi et al., 2018).

eccentricity by the encounter with the GSE merger.

The stellar mass of Gaia Enceladus has been estimated to be around $5 \times 10^8 M_\odot$ (see Helmi et al., 2018, Lane et al., 2023) while the accretion time is 10 Gyr (see Gallart et al., 2019, Fernández-Alvar et al., 2025). At that time, the mass ratio between the MW and GSE was about 1:4 (Helmi, 2020). This is why GSE is now considered as the latest significant merger event experienced by our Galaxy.

1.1.2 Sequoia

Another relevant merger event has been the one with Sequoia (Myeong et al., 2019). This has been discovered once again by analysing the IoM space, where an over-density of stars has been identified. These stars exhibit not only highly retrograde and energetic orbits, but also lower metallicities compared to those of Gaia Enceladus. Due to these properties, Sequoia was initially defined as in independent merging event.

Such a conclusion was then questioned by a detailed dynamical analysis in H. H. Koppelman et al., 2020. There, the authors simulated the merger event with Gaia-Enceladus, to find out that the dwarf galaxy is effectively destroyed at different times, during each peri-centric passage around the Milky Way. In such a process, the first stars to have been lost were the most external ones, that according to these N-body simulations end up in the same region of the IoM space populated by Sequoia. On top of that, since existing dwarf galaxies are commonly characterised by a radial metallicity gradient (e.g. Tolstoy et al., 2009), the first stars to have been stripped by GSE should also be more metal-poor, just like what observed and interpreted as Sequoia. To verify that Sequoia is indeed an independent accretion event of a dwarf galaxy onto the Milky Way, it is necessary to investigate more in detail its chemical abundances (Matsuno et al., 2022). This technique, also known as chemical tagging, revealed a systematic and significant difference between the chemistry of GSE and Sequoia in terms of Na, Mg, Si, Ca, Ti, Cr, Mn, Ni, Zn, Y, and Ba, therefore confirming the independent nature of Sequoia as a past merger.

1.1.3 Thamnos

Thamnos, which was discovered by H. H. Koppelman et al., 2019, is a less prominent substructure with typically lower orbital energy located in the retrograde region of the IoM space. Its stellar mass has been estimated to be smaller than $5 \times 10^6 M_\odot$: the combination of this result with its location in the IoM space seems to suggest that Thamnos is the remnant of an old merging event. Unfortunately, though, the chemical information available today for this system are still not precise enough to understand whether these stars come from a unique rather than from two remnants (see Ceccarelli et al., 2024).

1.1.4 Helmi Streams

Moving to the prograde portion of the halo, the state of the art is more complicated because the contamination from the disk is stronger. Despite this, it is possible to notice two clear merger events, the first of which is the one with the progenitor of the Helmi streams. The Helmi streams have been discovered by Helmi et al., 1999 as two over-densities in the velocity space (see Fig.1.5). These have opposite values of vertical velocity, which means that these streams warp around the Milky Way and cross the disk in two opposite directions during their orbit. Thanks to *Gaia*, the number of stars that were discovered to be associated to the Helmi streams increased (H. H. Koppelman et al., 2019). This allows to investigate the metallicity distribution function on a more solid statistical ground. H. H. Koppelman et al., 2019 found that it peaks at [Fe/H]=-1.5 dex and that it shows a significant intrinsic spread. Isochrone fitting also revealed that the Helmi streams' stars are old (age>11 Gyr), and possibly show an intrinsic spread in age as well. These characteristics clearly indicate the Helmi streams' progenitor to be a dwarf galaxy. Based on the dynamics of the stars along the stream, its mass seems to be $\approx 10^8 M_\odot$, similar to Sequoia, and the accretion event probably happened around 6-9 Gyr ago.

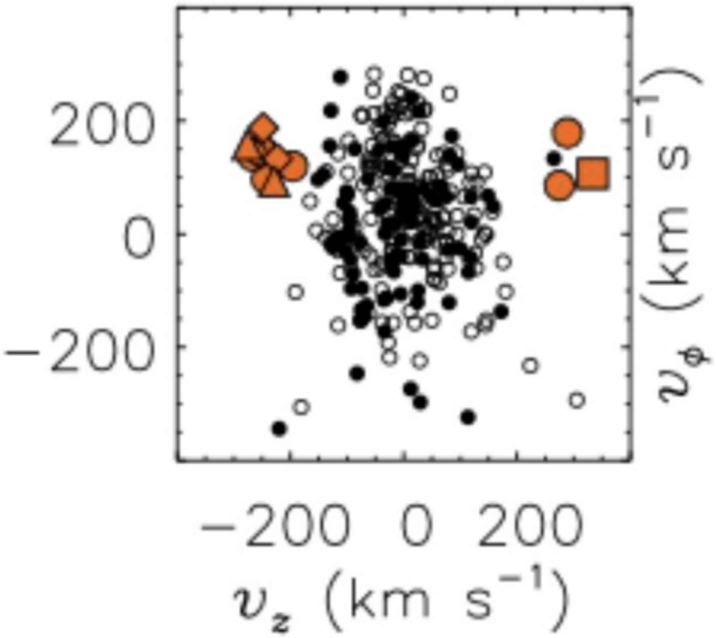

Figure 1.4: The velocity space used to identify the Helmi streams. It is here possible to recognise two different overdensities (in orange) characterised by opposite vertical velocities (see Helmi et al., 1999).

1.1.5 Sagittarius

Sagittarius is the latest accretion event so these stars haven't been affected by the phase mixing phenomenon yet, meaning that it is still possible to observe the spatial coherence on the plane of the sky. The mass of Sagittarius is quite debated and according to each work it varies in the range $M \in [10^8, 10^9]M_\odot$ (see Vasiliev and Belokurov, 2020) while the accretion time is quite well determined (6 Gyr ago) (Ruiz-Lara et al., 2022).

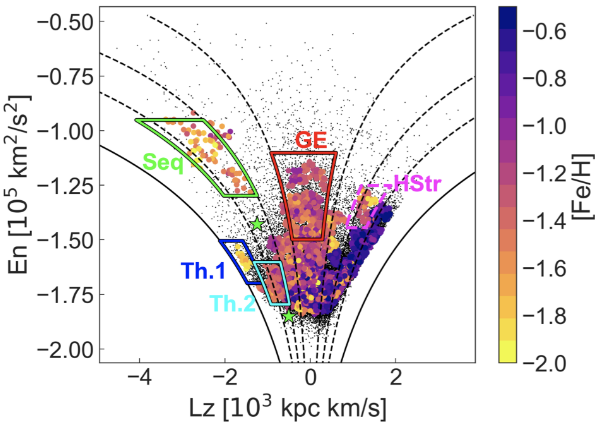

Figure 1.5: This plot represents where the debris of the past merger events are found in the IoM space. Inside the different boxes are the debris of GSE (in red), Sequoia (in green), the Helmi streams (in magenta) and Thamnos 1 and Thamnos 2 (in blue and cyan respectively) (plot taken from H. H. Koppelman et al., 2019).

1.2 Third data release of Gaia: increased precision implies increased complexity

Every new data release of *Gaia* improves the precision with which quantities are measured for all the stars observed in the previous data release. This means that every new data release increases the dynamical resolution in the IoM space, allowing the distinction of smaller stellar substructures originally associated with a common merger event. Specifically, in this paragraph the impact of the third data release of *Gaia* is described in the interpretation of the region of the IoM space corresponding to the Sequoia event.

1.2.1 Sequoia: more than one sub-structure

In particular, as highlighted in Fig.1.6, it is possible to notice that what was identified by Myeong et al., 2019 as a single over-density now splits in four separate sub-structures, depicted in blue, orange, cyan and magenta. Given this more detailed dynamical picture, it is now fundamental to understand whether all the four substructures correspond to independent merging events or not. The best way to answer this question is to use the chemical composition of these stars.

1.2.2 Antaeus and ED-3

The first effort in this sense has been performed by Ceccarelli et al., 2024, who analysed high-resolution spectra obtained with the UVES spectrograph (Dekker et al., 2000) in an homogeneous way, and compared highly precise abundance measurements for the aforementioned dynamical substructures. The most immediate conclusions were drawn about the two substructures called Antaues (Oria et al., 2022) and ED-3 (Dodd et al., 2023).

Antaeus is the clump of stars located in the most retrograde portion of the IoM space and it is shown with cyan symbols in Fig.1.6. On the other hand, ED-3 is the retrograde sub-structure represented with orange

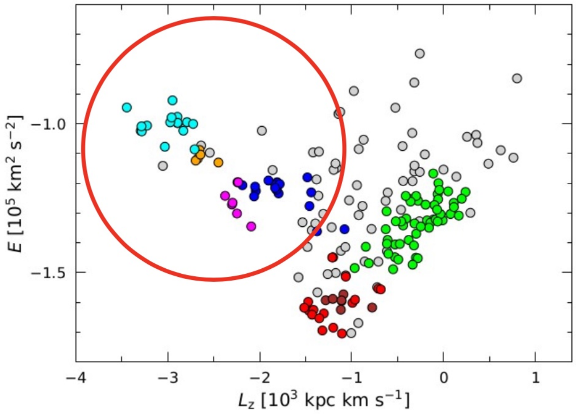

Figure 1.6: Position of a Galactic stellar sample in the energy vs vertical angular momentum space (plot taken from Dodd et al., 2023). In the region originally associated with the Sequoia accretion event (selected by the red circle), four substructures have been identified thanks to the *Gaia* DR3 and they are here represented in cyan, blue, orange and magenta.

symbols in Fig.1.6. Ceccarelli et al., 2024 focused on the chemical characterisation of these two stellar substructures and found that ED-3 shows elemental abundances that are always consistent with those of Antaeus. Since Antaeus and ED-3 are also very close to each other in the IoM space, the combination of dynamical and chemical properties suggests that these two clumps are actually part of the same relic. Since Sequoia behaves differently with respect to Antaeus and ED-3, the clump associated to this merger event is much smaller than originally thought and it is represented with blue symbols in Fig.1.6. Finally, the smallest clump called ED-2, represented with magenta symbols, deserves a separate investigation.

1.2.3 ED-2

Dodd et al., 2023 reported ED-2 as an independent group which is compact in velocity too. The compactness in the velocity space indicates that this structure is not phase mixed yet, meaning that its stars stream together through the solar neighbourhood. By plotting the CMD for ED-2 members using the third data release of *Gaia*, Balbinot et al., 2023 noticed two important results. The first is that, looking at the Red Giant Branch (RGB) width, the CMD was found to be consistent with a single stellar population. The second is that even though the age is not well constrained, because the Main Sequence Turn Off (MSTO) is not well populated, the only way to reproduce the colour of the RGB and the main sequence is to have a very old stellar population with $\log(age/yr) = 10.20$.

The fact that ED-2 seems to be composed photometrically by a single, old stellar population raised questions on its nature. Usually, dynamical substructures represent disrupted dwarf galaxies, but the photometric features of ED-2 are consistent with a globular cluster nature, too.

To better understand the nature of this sub-structure, Balbinot et al., 2023 investigated 22 stellar members of ED-2 that were bright enough to have metallicities measured by ground based surveys (specifically LAMOST and APOGEE providing low and medium resolution spectra). On the other hand, Ceccarelli et al., 2024 and Dodd et al., 2025 worked with high resolution spectra taken with UVES and PEPSI, but for a very low number of stars (4 and 5 respectively). These three works tried to establish the nature of ED-2's progenitor by studying the most striking chemical difference between globular clusters and dwarf galaxies which is the metallicity distribution function (MDF). Indeed, this is expected to be consistent with a null intrinsic scatter in the case of a globular cluster (see Gratton et al., 2004), while it is expected to be much broader in the case of a dwarf galaxy (see Tolstoy et al., 2009). All these three previous works found evidence that the MDF obtained by analysing ED-2 stars is very narrow (see Fig.1.7), which seems to suggest that the progenitor system is a globular cluster that was accreted onto the Milky Way. Nevertheless, due to either the low statistics or the low resolution employed in Balbinot et al., 2023, Ceccarelli et al., 2024 and Dodd et al., 2025 this evidence is not conclusive. Yet, it is of fundamental importance to understand the nature of ED-2, as the history of the build-up of the Milky Way halo would be influenced in a very different way. For example, a typical dwarf galaxy would contribute 2 orders of magnitude more than a GC to the total halo mass budget (McLaughlin and van der Marel, 2005). The main goal of this project is hence to conclusively establish ED-2 progenitor's nature, by surpassing the two main limitations of the previous works, that is by taking advantage of high resolution spectra for a large sample of targets.

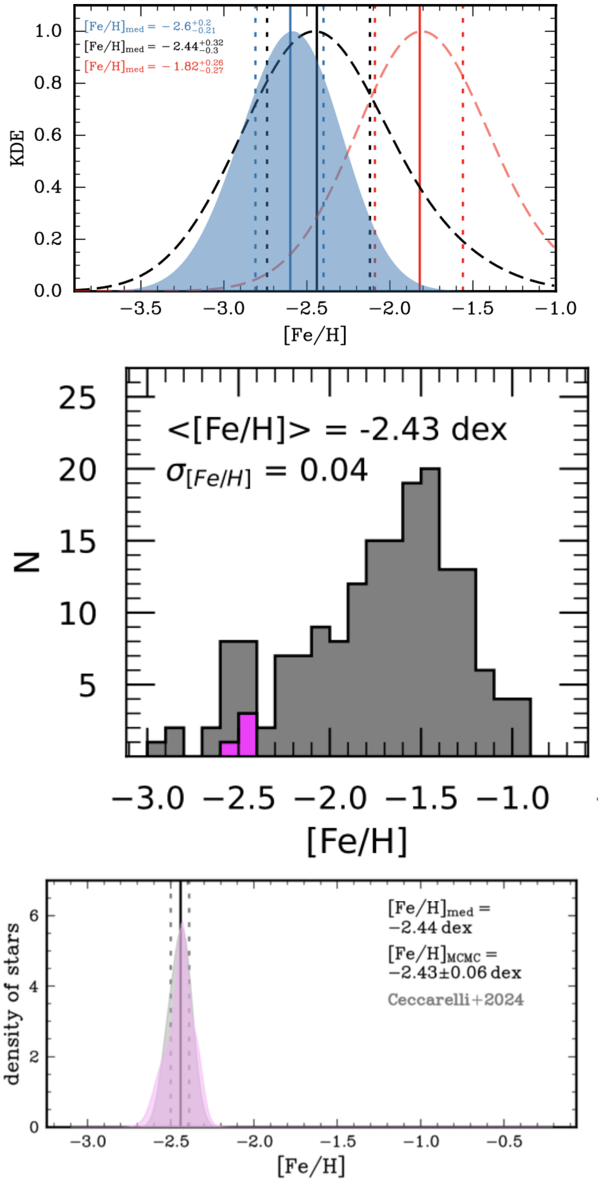

Figure 1.7: In this figure the metallicity distribution functions for ED-2 obtained from previous works are represented. First, the metallicity distribution function obtained by Balbinot et al., 2023, then the one obtained by Ceccarelli et al., 2024 and finally the one obtained by Dodd et al., 2025.

Chapter 2

Target stars and stellar parameters

2.1 Target stars

This work aims at studying the chemical composition of 24 stars dynamically associated to the stellar substructure known as ED-2. This substructure was first discovered by Dodd et al., 2023 where the authors applied the clustering algorithm described by Ruiz-Lara et al., 2022 to the three-dimensional IoM space of energy, z and the perpendicular components of the angular momentum (E, L_z, $L_\perp$). Taking as reference the catalogue provided by Dodd et al., 2023, the position of ED-2 member stars in the IoM space can be appreciated in Fig.2.1 where they are represented by the blue points.

For high-resolution spectroscopic observations we selected ED-2 members following the associations identified by Balbinot et al., 2023. To minimize exposure times while still obtaining high signal-to-noise ratio (S/N or SNR) spectra, we restricted the selection to stars with magnitudes brighter than V = 15.2. Our sample includes 17 proprietary high-resolution spectra obtained with UVES and PEPSI for all stars in their catalogue that have not yet been observed with high-resolution spectrographs. The sample is further complemented by 4 spectra retrieved from the ESO archive (previously analysed by Ceccarelli et al., 2024 and Dodd et al., 2025) and 3 spectra from the LBT archive (Ceccarelli et al., 2024). In total, our final dataset comprises 24 ED-2 stars, representing the largest high-resolution spectroscopic sample of this stellar system currently available in the literature. The main information about the observed targets are listed in Tab.2.3, Tab.2.4, Tab.2.5 and Tab.2.6.

Among the 24 stars that make up our sample, 8 stars have been observed using UVES spectrograph at the Very Large Telescope (VLT) of ESO (Dekker et al., 2000) in Chile and 16 stars have been observed using the PEPSI spectrograph at the Large Binocular Telescope (LBT) in Arizona (Strassmeier et al., 2015).

PEPSI observations have been performed with the CD3 grating for the Blue Arm, with a spectral coverage of [4800, 5440] Å, the CD4 and CD6 gratings for the Red Arm with a spectral coverage of [5364, 6321] Å and [7410, 9140] Å respectively, all with a spectral resolution of 50000. The choice of this set-up for the two arms was dictated by the trade-off between the access to measurable lines, allowing to derive the abundance of scientifically relevant chemical elements, and the efficiency of the spectrograph with the goal of achieving S/N $>$ 30 for a reliable measure of the chemical abundances we are interested in. The spectra have been reduced with the dedicated PEPSI pipeline, which contains bias subtraction, flat-fielding,

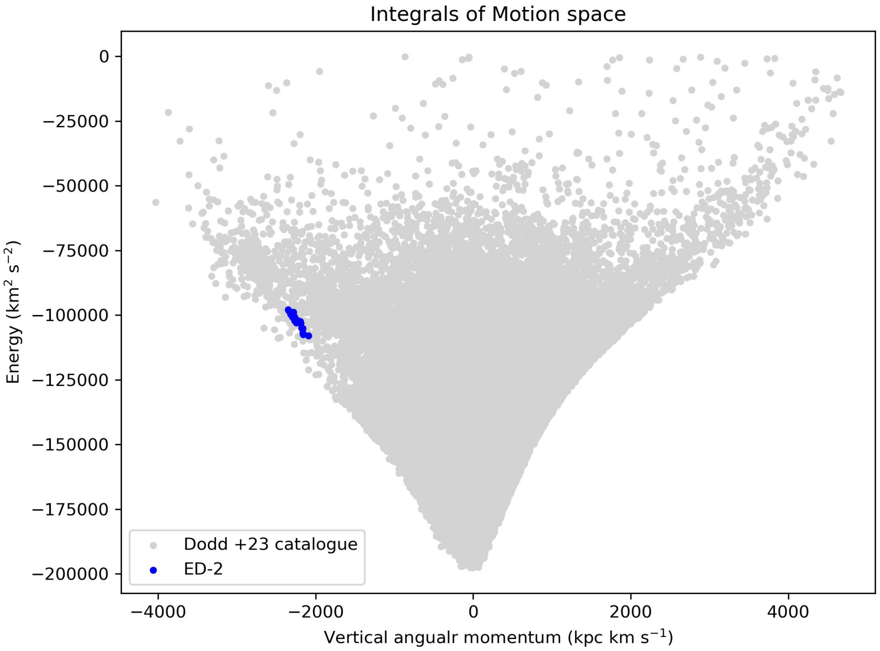

Figure 2.1: IoM space where the energy is plotted as a function of the vertical angular momentum. Among all the stars listed in the catalogue provided by Dodd et al., 2023 represented in grey, ED-2 member stars are represented by the blue points.

spectral extraction, order merging, wavelength calibration and normalization. The observations of close sky region in the same exposure times of the targets have been executed in order to subtract the sky contribution to the stellar spectra.

For what instead concerns the stars observed with UVES, the observations were performed in Dichroic mode adopting the standard settings Dic 1 Blue Arm CD2 390 ([3600, 4800] Å) and Dic 1 Red Arm CD3 564 ([4800, 6600] Å) and with the 1"×12" slit, thus yielding a resolution of 40000. All the observed spectra have then been reduced with the ESO pipeline including the same steps described above for the PEPSI pipeline. The sky subtraction has been performed by using the sky spectrum extracted from the same slit.

2.1.1 Inspection of the target spectra

The first step in a spectroscopic analysis is the inspection of the target spectra, during which it is fundamental to check whether the first and/or last pixels could provide a number of counts equal to zero. If this happens, it is necessary to exclude those pixels by selecting only the region of the spectrum that does not present this feature.

The exclusion of these zero count pixels is necessary because they give some problems in the normal-

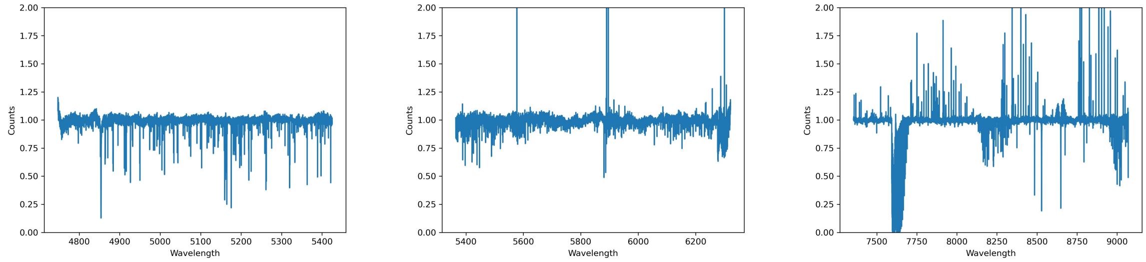

(a) *CD3* channel with spectral coverage [4747, 5424] Å

(b) *CD4* channel with spectral coverage [5364, 6321] Å

(c) *CD6* channel with spectral coverage [7355, 9069] Å

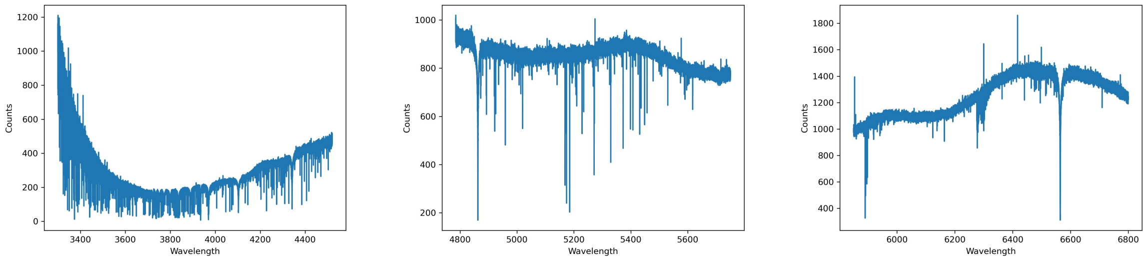

(d) *blue* channel with spectral coverage [3300, 4520] Å

(e) *redl* channel with spectral coverage [4785, 5750] Å

(f) *redu* channel with spectral coverage [5850, 6800] Å

Figure 2.2: Examples of PEPSI *CD3*, *CD4* and *CD6* spectra for the target star4 (upper panels) and of UVES *490*, *low 580* and *up 580* spectra for the target star23 (lower panels).

isation procedure which is carried out in order to work, in the following steps, with a flat and normalised to unity spectrum. As a matter of fact, the normalised spectrum is needed because to obtain the chemical abundances a comparison between the observed and the synthetic spectra is required. Since the synthetic spectra are normalised to unity, this comparison can be carried out only if also the observed spectrum presents this specific feature, otherwise the best match, which provides the chemical abundances, between the observed and the synthetic spectrum is never obtained. Formally, there are different approaches in order to normalise the spectrum and in particular the one employed in this first inspection of the available spectra is the median smoothing technique. In this case the spectrum is divided in several small regions identified by the `width` parameter which must be an odd number and it establishes the number of pixels inside each small region. In order to normalise the observed spectrum, first it is necessary to obtain a fit that describes the general behaviour of the spectrum, then the normalised spectrum is simply defined as the original observed spectrum divided by the fit. In particular, in the determination of the fit that best describes the behaviour of the observed spectrum, the `width` parameter must be large enough so that the single regions are not affected by the presence of lines.

The last step in the inspection of the spectra consists in the determination of the signal-to-noise ratio. The SNR is needed in order to quantify the quality and precision of the observations and, intuitively, is defined as the ratio between the signal, which is the amount of counts coming from the source, divided by the noise, which takes into account all sources of uncertainty. Generally, there are three main sources of fluctuations that determine the noise:

- Poissonian noise related to source counts which, by definition, follow a Poissonian distribution, so σ_S is the square root of the number of counts coming from the source ($\sigma_S = \sqrt{S}$);
- Poissonian noise related to counts coming from the sky background, so σ_B is the square root of the number of counts coming from the sky background ($\sigma_B = \sqrt{B}$);
- Red out noise (RON) which is due to an instrumental effect and it does not follow a Poissonian distribution.

These three sources of uncertainty are independent one from the other so in the definition of the noise it is possible to simply sum in quadrature their contributions, meaning that the SNR is defined as follows:

$$SNR = \frac{S}{\sqrt{\sigma_S^2 + \sigma_B^2 + RON^2}} \tag{2.1}$$

In other words, the SNR is a measure of the Poissonian noise of the given spectrum which can be estimated by considering a large region of the normalised spectrum without any emission or absorption lines. Once this region has been identified, the SNR is given by the average value of counts in this region divided by the standard deviation of the signal.

2.2 Gaia DR3 photometry

In order to derive the stellar parameters of the target stars, as described below, we used the information provided by Gaia DR3 photometry (see ESA Gaia Archive, 2025, Gaia Collaboration et al., 2016 and Gaia Collaboration et al., 2023). Some key quantities are: right ascension, declination angle, parallax with its corresponding error and the three (G, BP, RP) observed magnitudes with their corresponding *flux/error*, which provide the error associated to the observed magnitudes through the following relation:

$$\sigma = \frac{1.086}{flux/error} \tag{2.2}$$

Although Gaia, in principle, provides absolute parallaxes, imperfections in the instrument and data-reduction process introduce systematic biases in the published values. To correct for this effect, we have applied the zero-point correction proposed by Lindegren et al., 2021 and subtracted this value to the measured parallax. The corrected value of the parallax can then be used to compute the distance of the target star as 1000/parallax (see Tab.2.4).

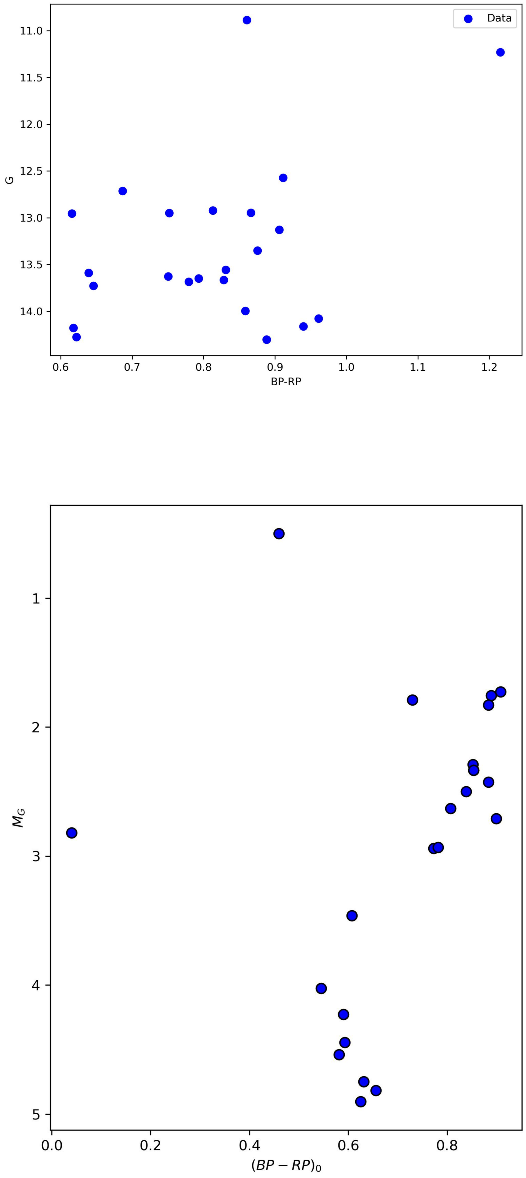

Figure 2.3: *Top panel*: Observed BP-RP vs G colour-magnitude diagram of the 24 stars analysed in this project. *Bottom panel*: Intrinsic colour magnitude diagram of the 24 stars analysed in this project (magnitudes corrected for the extinction phenomenon).

Another fundamental quantity that should be gathered in this preliminary part of the analysis is the extinction parameter in the V band (A_V) which, through Eq. 2.5, will provide the colour excess needed in the computation of the effective temperature. To obtain A_V the `G-TOMO` tool of the EXPLORE platform (see EXPLORE Consortium, 2021) has been employed. This requires as input parameters only three quantities: right ascension, declination angle and distance of the target star expressed in parsecs. By submitting the query it provides the cumulative extinction curve which gives rise to two possible outcomes as it can be appreciated in Fig.2.4. Either the value of A_V falls exactly on this curve or it is extrapolated whenever the distance that characterises the star overcomes the limit guaranteed by this platform.

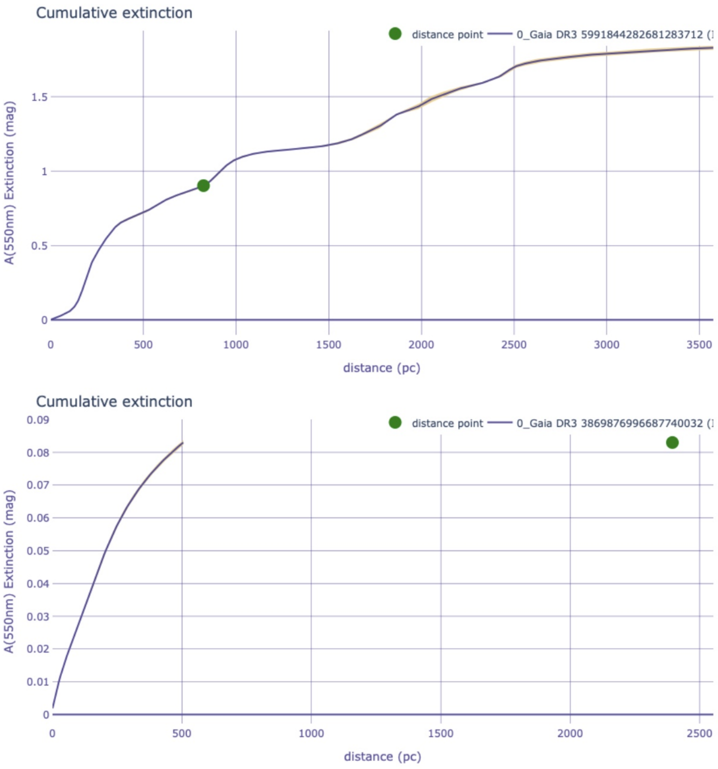

Figure 2.4: In the *top panel* the target star has an extinction parameter that lies on the extinction curve, while in the *bottom panel* the target star has an extinction parameter that does not lie on the curve and in this case the maximum value of A_V is taken as output of the tool, hence an extrapolation is performed by the `G-TOMO` tool of the explore platform.

2.3 Effective temperature

For what concerns the effective temperature (T_{eff}), its computation starts with the observed colour, which usually does not coincide with the intrinsic one because of the extinction phenomenon. This effect implies that there is a difference between the observed apparent magnitude m_λ and the intrinsic apparent magnitude $m_{\lambda,0}$ and in particular that the Eq.2.3 is valid:

$$m_\lambda = m_{\lambda,0} + A_\lambda \tag{2.3}$$

where A_λ is defined as *extinction parameter* and it has a strong dependence, described by the *extinction law*, on the wavelength λ. In particular, since large magnitudes correspond to faint objects, the extinction makes the star appear fainter than it really is.

The first step is therefore to correct the observed colour for the extinction effect obtaining the intrinsic colour. To do this, the definition of *colour excess* must be provided and it must be adjusted to the analysed case. Specifically, by applying Eq.2.3 to the B and V bands, Eq.2.4 is obtained

$$(B-V)_0 = (B-V) - (A_B - A_V) \tag{2.4}$$

where $(B-V)$ is the observed colour, given simply by the difference between the observed magnitudes in B and V bands, $(B-V)_0$ is the intrinsic colour and $(A_B - A_V)$ is the colour excess previously mentioned and usually indicated as $E(B-V)$.
Knowing that $A_B = 1.32A_V$ and substituting this result in the definition of colour excess, the relation between the extinction parameter and the colour excess can be obtained:

$$A_V = R_V E(B-V) \tag{2.5}$$

where $R_V = 3.12$. Since this result is valid at all wavelengths, the general formula is $A_\lambda = R_\lambda E(B-V)$ where

$$R_\lambda = R_V \frac{A_\lambda}{A_V} = R_V k_\lambda \tag{2.6}$$

This theoretical treatment is needed because Gaia provides magnitudes in the G, BP and RP bands so to obtain the intrinsic colour Eq.2.4 can be applied and it becomes

$$(BP-RP)_0 = (BP-RP) - E(BP-RP) \tag{2.7}$$

with $E(BP-RP) = A_{BP} - A_{RP}$. To compute then k_λ, we have employed three equations:

$$k_\lambda = a_1 + a_2X + a_3X^2 + a_4X^3 + a_5A_V + a_6A_V^2 + a_7A_V^3 + a_8A_VX + a_9A_VX^2 + a_{10}XA_V^2 \tag{2.8}$$

where $\lambda =$ G, BP, RP depending on the chosen band, X is the colour and a_i are constants which have different values depending on λ and depending on whether the target is a giant rather than a dwarf star (see ESA Gaia Collaboration, 2021). Starting from the k_λ and using the relations presented so far, it is possible to compute the corresponding R_λ, the extinction parameters and $E(BP-RP)$.
Formally, this is an iterative procedure, in the first run the variable X is set to be the observed colour, all the quantities are computed and this results in a first corrected colour. This is then used as input for the second iteration and the procedure is carried out until the convergence is reached, hence until the difference between the final corrected colour and the one used as variable X in the latest iteration is smaller than a tolerance (in this case fixed to 10^{-4}).

Once the intrinsic colour has been obtained, it is possible to compute the effective temperature starting from the Boltzmann factor ($\theta = 5040/T_{eff}$), which has been defined by Mucciarelli et al., 2021 as follows:

$$\theta = b_0 + b_1C + b_2C^2 + b_3[Fe/H] + b_4[Fe/H]^2 + b_5[Fe/H]C \tag{2.9}$$

where b_i are constants which depend on the intrinsic colour used ($(BP-RP)_0$ in this case) and on whether the target is a giant or a dwarf star (see Tab.2.1), while $[Fe/H]$ is the metallicity of the star. In this work, the value $[Fe/H] = -2.44$ dex obtained by Dodd et al., 2025 was used for all stars. This choice is justified by the fact that, as discussed in the introduction, previous studies have found a very narrow metallicity distribution function for ED-2 stars, suggesting that they were stripped from a globular cluster. Such systems are known to exhibit a remarkably homogeneous chemical composition, meaning that all member stars share essentially the same metallicity. Therefore, adopting a constant value of $[Fe/H] = -2.44$ dex for all stars in Eq. 2.9 is a reasonable and physically motivated assumption. We then noticed that the measured metallicity is not significantly different from the literature value used in Eq. 2.9, and therefore there is no need to recompute everything, as the dependence on [Fe/H] is weak.

Intrinsic colour	b_0	b_1	b_2	b_3	b_4	b_5
$(BP - RP)_{0,giant}$	0.5323	0.4775	-0.0344	-0.0110	-0.0020	-0.0009
$(BP - RP)_{0,dwarf}$	0.4929	0.5092	-0.0353	0.0192	-0.0020	-0.0395

Table 2.1: Coefficients of the (Bp-Rp)-theta relation for giant. and dwarf stars (Mucciarelli et al., 2021)

2.3.1 Uncertainties in the computation of the effective temperature

In the computation of the effective temperature through the relation provided by Mucciarelli et al., 2021 there are three sources of uncertainties, the dominant one related to the uncertainty of the adopted calibration. In particular, to quantify this term we have taken as reference the work of Ceccarelli et al., 2024, where $\delta T =$ 60-80 K for giant and dwarf stars respectively. Secondly, we must take into account the uncertainty associated to the colour BP-RP. These observed magnitudes have their corresponding errors so that the error associated to the observed colour is the sum in quadrature of the errors associated to the two magnitudes:

$$\delta_{BP-RP} = \sqrt{\delta_{BP}^2 + \delta_{RP}^2} \tag{2.10}$$

This has brought us to study how much the effective temperature changes if we consider as input the $(BP - RP) \pm \delta_{BP-RP}$ instead of the observed colour. This variation of T_{eff} must then be summed in quadrature to the δT of 60-80 K previously mentioned because these effects are independent one from the other.

In addition to this, also the uncertainty in the extinction parameter A_V has an impact in the determined T_{eff}. This parameter was obtained thanks to the `G-TOMO` tool of the EXPLORE platform. The problem that rises from the employment of this tool is that it is able to provide an exact value of A_V only for sources within 800 pc from the observer, meaning that for all the sources which are further away it extrapolates the extinction curve so that also the value of A_V could be wrong. Since the extinction parameter and the colour excess are strictly linked one to the other, we have made a conservative assumption: we assumed that there is a 20% level of uncertainty associated with the colour excess $E(B-V)$. So, just like it has been done for the observed colour, also in the case of $E(B-V)$ we have studied how the effective temperature changes by considering $E(B-V) \pm \delta E(B-V)$ instead of $E(B-V)$. Once again the variation in T_{eff} must be summed in quadrature to the previous two variations because we are still dealing with independent effects.

2.4 Surface gravity

Surface gravity is given by $\log(g)$ with $g = GM/R^2$ where $G = 6.67259 \times 10^{-11} Nm^2/kg$ is the gravitational constant, M is the stellar mass and R is the stellar radius.

R^2 can be derived from the Stefan-Boltzmann equation:

$$L = 4\pi\sigma R^2 T_{eff}^4 \tag{2.11}$$

where $\sigma = 5.67 \times 10^{-8} W/m^2K^4$ is the Stefan Boltzmann constant and T_{eff} is the effective temperature obtained in the previous step. R^2 is the only unknown because starting from the observed magnitude in the G band we can obtain the luminosity. To pass from the observed magnitude in the G band to the luminosity, the so-called *translator* can be used.

First, using Eq.2.3, we can obtain the apparent intrinsic magnitude. Then, using the definition of the distance modulus

$$(m - M)_0 = 5\log(d_{pc}) - 5 \tag{2.12}$$

the absolute intrinsic magnitude (M) is obtained. Subsequently, we can use the bolometric correction, defined as $BC_\lambda = M_{bol} - M_\lambda$, to pass from the absolute magnitude in a given band M_λ to the bolometric magnitude M_{bol}. In particular, the expression for the bolometric correction has been obtained by Andrae et al., 2018:

$$BC_G(T_{eff}) = \sum_{i=0}^{4} a_i (T_{eff} - T_{eff,\odot})^i \tag{2.13}$$

where $T_{eff,\odot} = 5772$ K is the effective temperature of the Sun and a_i are numerical coefficients that, for $T_{eff} > 4000$ K, are reported in Tab.2.2. Finally, to obtain the luminosity of the given star, it is necessary to apply the following relation:

$$M_{bol} - M_{bol,\odot} = -2.5\log\left(\frac{L}{L_\odot}\right) \tag{2.14}$$

where $M_{bol,\odot} = 4.72$ is the bolometric magnitude of the Sun while $L_\odot = 3.832 \times 10^{33}$ erg/s is the solar luminosity. Once the luminosity is obtained, Eq.2.11 can be applied and the resulting R^2 is substituted in the definition of $\log(g)$.

	a_0	a_1	a_2	a_3	a_4
BC_G	6.0×10^{-2}	6.731×10^{-5}	-6.647×10^{-8}	2.859×10^{-11}	-7.197×10^{-15}

Table 2.2: Coefficients for the BCG-T_{eff} relation.

In the definition of $\log(g)$ though, there's also the stellar mass M, which is obtained from the best-fit theoretical isochrone. In this project, the BASTI isochrones have been employed (see Pietrinferni et al., 2021). We assumed $[Fe/H] = -2.44$ dex, alpha-enhanced chemical mixture, an age of 13.5 Gyr (according to Dodd et al., 2025) and the Gaia DR3 photometric system. Fig.2.5 shows the final mass provided by Pietrinferni et al., 2021 as a function of the logarithm of the luminosity: depending on the value of the luminosity obtained in the previous step, for each star the value of the mass is obtained. Specifically, $M = 0.72M_\odot$ for dwarf stars and $M = 0.8M_\odot$ for giant stars are the values found for our target stars.

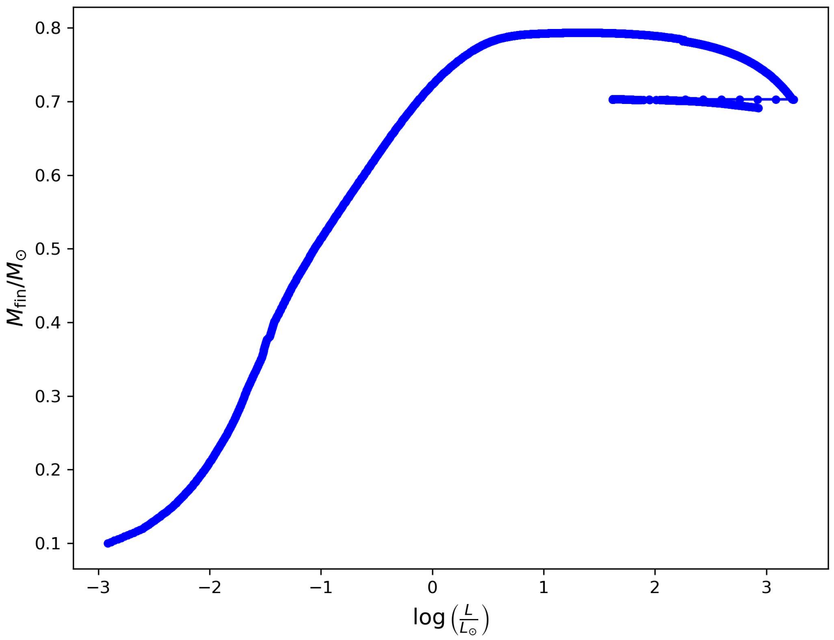

Figure 2.5: Final stellar mass in solar units obtained from the `BASTI` isochrone with age=13.5 Gyr and [Fe/H]$= -2.44$ dex as a function of the logarithm of the stellar luminosity normalised by the solar value.

2.5 Kiel Diagram

Considering how effective temperature and surface gravity have been obtained, we can plot the observed targets in the Kiel diagram (see Fig.2.6). Here we have represented in red all the stars observed with PEPSI and in blue those observed with UVES. For completeness, we have also superposed to the data points a BASTI isochrone characterised by an age of 13.5 Gyr, metallicity of -2.44 dex (results obtained by Dodd et al., 2025) and α enhancement of +0.4. Thanks to this plot, it's easy to notice that our sample is made of 16 giant stars and 8 dwarf stars.

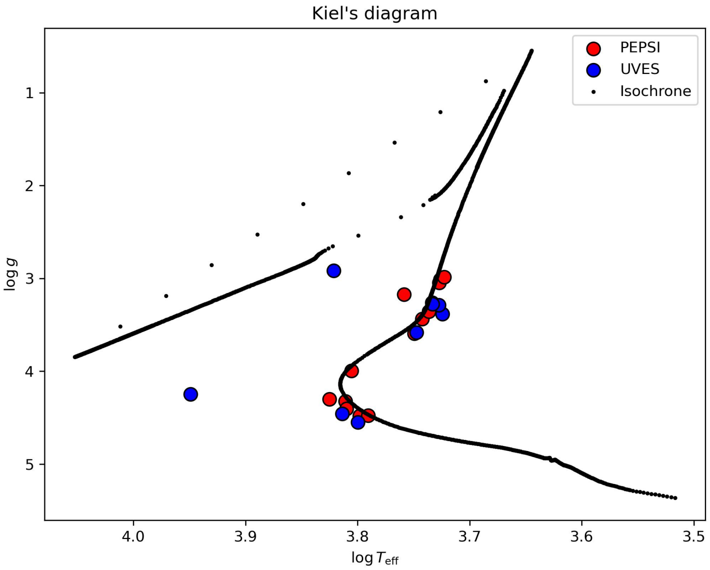

Figure 2.6: Kiel's diagram with an isochrone (in black) superimposed to the position of the observed targets (red for PEPSI and blue for UVES). The isochrone in black also allows to appreciate the different evolutionary stages' velocities.

2.5.1 Gaia DR3 4137395670479268352: the hottest star in the sample

From the Kiel's diagram it is possible to highlight the presence in our sample of a very hot star, which is star19 (see Tab.2.3), characterised by an effective temperature T_{eff} = 8894 K. This star is so hot that its spectrum, as it can be appreciated in Fig.2.7, presents only Balmer lines and telluric lines. For this reason we cannot obtain chemical abundances for this star. The only information that can be gathered is the radial velocity though cross correlation technique (see Sect.4.2).

This star is dynamically associated with ED-2 and it seems to be a blue horizontal branch star. To justify the fact that ED-2 presents also a blue horizontal branch, a more theoretical treatment is needed. The position of stars along the horizontal branch (HB) is mainly established by the q parameter which is defined as the ratio between the core mass and the total mass of the star during this specific evolutionary stage. At this point there are two results that have already been mentioned and that allow us to explain the extension to the blue of the HB. The first result is that ED-2 stars represented in the Kiel's diagram are best fitted by a BASTI isochrone of 13.5 Gyr. This, which is a result that was also found by Dodd et al., 2025, means that we are dealing with low mass stars, which is confirmed by the determination of stellar masses that was necessary in order to compute the surface gravity for each of the targets. As a direct consequence of this, the stars in our sample all experience the He flash in their core meaning that the mass of the core in the definition of the q parameter is going to be 0.5 $M_\odot$ for all of them, so the total mass of the star will be the quantity establishing the position of those stars along the HB. Considering that these are low mass stars, for a fixed core mass, also the envelope of the star is necessarily characterised by a very low mass. This implies that the thermonuclear activity happening in the innermost regions of the stellar structure easily heats up the envelope. The high T_{eff} reached brings the star to the blue side of

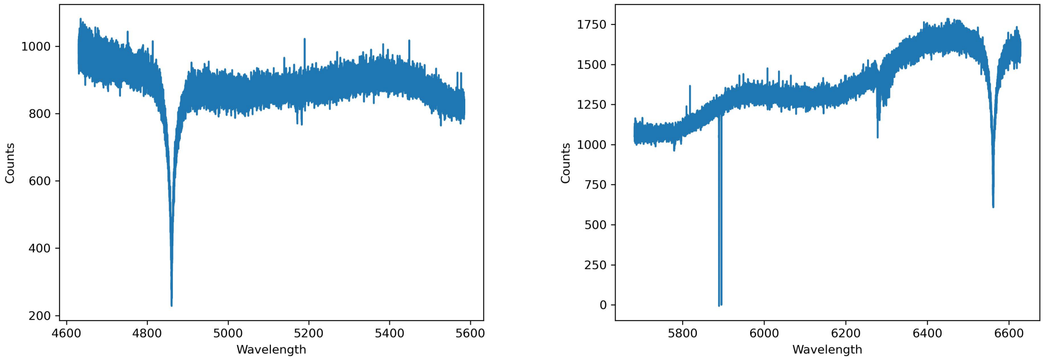

Figure 2.7: Spectrum of star19 in the *redl* wavelength range on the *left* and spectrum of star19 in the *redu* wavelength range on the *right*.

the HB. In addition to this, the total mass of the star depends strongly on the metallicity. Previous works found this to be a very metal poor cluster of stars, which implies that its stars are expected to have low masses. In conclusion, the stars that we are dealing with are characterised by a small total mass not only because of their age but also because of their metallicity and the small values of M_{tot} allow the existence of blue HB stars in the case of ED-2.

2.5.2 Gaia DR3 5991844282681283712: red HB star

Star15 (see Tab.2.3), which, based on its position in both the CMD and in the Kiel's diagram, is defined as a red HB star, has been another peculiar case. This star has been difficult to analyse with `4dao` simply because it is already hot enough ($T_{eff} = 6628$ K) to provide a spectrum that, just like in the case of star19 (see Tab.2.3), is characterised mainly by Balmer and telluric lines, so even in this case `4dao` encounters some difficulties and hence the radial velocity obtained with `4dao` has been checked using the cross correlation technique (see Sect.4.2).

Gaia ID	name	spectrograph
Gaia DR3 3951060094855048960	star1	PEPSI
Gaia DR3 3992080193627189632	star2	PEPSI
Gaia DR3 759407156314566784	star3	PEPSI
Gaia DR3 1693676308288915712	star4	PEPSI
Gaia DR3 1577319631286280960	star5	PEPSI
Gaia DR3 1578782394069199488	star6	PEPSI
Gaia DR3 1698151522476505344	star7	PEPSI
Gaia DR3 3869876996687740032	star8	PEPSI
Gaia DR3 779616592350301952	star9	PEPSI
Gaia DR3 1298276602498467072	star10	PEPSI
Gaia DR3 4532592619428218624	star11	PEPSI
Gaia DR3 4245522468554091904	star12	PEPSI
Gaia DR3 5444820480268295424	star13	UVES
Gaia DR3 3549718318990080896	star14	UVES
Gaia DR3 5991844282681283712	star15	UVES
Gaia DR3 6632335060231088896	star16	UVES
Gaia DR3 3869876996687740032	star17	UVES
Gaia DR3 4479226310758314496	star18	UVES
Gaia DR3 4137395670479268352	star19	UVES
Gaia DR3 3915925991063287808	star20	PEPSI
Gaia DR3 3963873700285600128	star21	PEPSI
Gaia DR3 4008274384997266560	star22	PEPSI
Gaia DR3 6746114585056265600	star23	UVES
Gaia DR3 4318465066420528000	star24	PEPSI

Table 2.3: Stellar information taken from the Gaia DR3: for every star the Gaia ID, a reference name and the instrument used to observe the specific target star are provided.

name	RA	DEC	Parallax (mas)	Distance (pc)
star1	182.0405481644398	19.920933510340728	1.81±0.02	552.5±6.20
star2	169.61606498184224	23.437512872525463	0.668±0.018	1496.70±39.30
star3	171.32881358828294	35.31272592009054	0.60±0.02	1670.91±65.22
star4	224.11678768559287	67.78193429532448	0.70± 0.01	1426.10±20.86
star5	193.3106331607195	58.02767219375996	0.512±0.013	1954.55±51.04
star6	195.42808638431356	59.35577421797703	0.736±0.013	1359.14±24.47
star7	217.05033218957834	70.57239217997619	0.627±0.010	1595.49±26.71
star8	159.4981130696763	9.198975464267646	0.42±0.02	2394.30±119.02
star9	159.9443366484265	40.716550804114505	0.561±0.017	1781.34±54.33
star10	246.10322003040403	21.667429642909003	2.690±0.013	371.75±1.75
star11	280.59738137109497	22.783934375672008	1.999±0.014	500.36±3.48
star12	307.6327712050222	4.515233884236154	1.261±0.019	792.90±11.98
star13	160.3515014072711	-33.31704027409937	0.56±0.02	1771.08±68.64
star14	164.27066111466112	-22.25080950591425	0.47±0.02	2108.14±108.63
star15	241.54965201743187	-43.31913896293447	1.214±0.018	823.94±12.48
star16	286.5301287007258	-60.496593537997875	1.08±0.02	928.66±17.46
star17	159.4981130696763	9.198975464267646	0.42±0.02	2394.30±119.02
star18	277.96005767229116	8.598236141137342	2.613±0.017	382.62±2.55
star19	263.7027959563528	-13.99080256676846	1.599±0.019	625.30±7.59
star20	174.8934486540262	10.183097228038575	0.93±0.02	1029.40±21.10
star21	170.97030869906405	11.522058115425414	0.97±0.02	990.98±24.36
star22	185.24675689787594	24.99319312160748	1.12±0.02	863.67±14.00
star23	291.83853579807584	-31.886092167200175	1.98±0.02	493.59±4.41
star24	294.82786250815144	14.930979608612361	1.64±0.07	595.33±24.46

Table 2.4: Stellar information taken from the Gaia DR3: for every star the reference name, the right ascension, the declination angle, the parallax and the distance are hereby provided.

name	G (mag)	BP (mag)	RP (mag)	Intrinsic colour	E(B-V)
star1	13.6848±0.0002	13.9870±0.0008	13.2078±0.0009	0.7531±0.0012	0.019
star2	13.5559±0.0003	13.8819±0.0011	13.0507±0.0008	0.8067±0.0014	0.019
star3	12.9505±0.0004	13.2394±0.0008	12.4874±0.0005	0.730±0.001	0.017
star4	12.5717±0.0002	12.9354±0.0007	12.0241±0.0005	0.8891±0.0008	0.017
star5	13.9969±0.0002	14.3357±0.0011	13.4771±0.0008	0.8382±0.0014	0.015
star6	13.6474±0.0002	13.9552±0.0006	13.1621±0.0006	0.7727±0.0008	0.015
star7	13.3510±0.0002	13.6985±0.0008	12.8232±0.0005	0.852±0.001	0.018
star8	14.3018±0.0003	14.6547±0.0011	13.7662±0.0009	0.8535±0.0014	0.03
star9	13.1286±0.0002	13.4896±0.0007	12.5838±0.0006	0.8838±0.0009	0.017
star10	12.7140±0.0002	12.9745±0.0005	12.2878±0.0004	0.6314±0.0006	0.04
star11	13.6645±0.0002	13.9868±0.0008	13.1586±0.0004	0.6560±0.0009	0.13
star12	13.7266±0.0002	13.9685±0.0009	13.32268±0.0008	0.5450±0.0012	0.07
star13	14.0770±0.0002	14.4662±0.0010	13.5051±0.0007	0.8994±0.0012	0.05
star14	14.1622±0.0002	14.5399±0.0013	13.6002±0.0008	0.8834±0.0016	0.04
star15	10.887±0.007	11.20±0.03	10.34±0.02	0.46±0.03	0.3
star16	12.9456±0.0003	13.2876±0.0007	12.4213±0.0004	0.7818±0.0008	0.06
star17	14.3018±0.0003	14.6547±0.0010	13.7662±0.0009	0.8535±0.0014	0.03
star18	12.9231±0.0003	13.2411±0.0006	12.4282±0.0006	0.5813±0.0008	0.17
star19	12.9537±0.0003	13.1869±0.0011	12.5714±0.0006	0.0406±0.0012	0.4
star20	13.5879±0.0003	13.8264±0.0015	13.1874±0.0011	0.607±0.002	0.02
star21	14.2736±0.0003	14.5046±0.0015	13.8826±0.0014	0.590±0.002	0.02
star22	14.1779±0.0002	14.4064±0.0016	13.788±0.001	0.593±0.002	0.018
star23	13.6258±0.0002	13.9133±0.0011	13.1627±0.0009	0.6253±0.0015	0.09
star24	11.2311±0.0003	11.7539±0.0008	10.5382±0.0008	0.9079±0.0009	0.2

Table 2.5: Stellar information taken from the Gaia DR3: for every star the reference name together with the observed magnitudes in G, BP and RP bands, intrinsic colour and colour excess are hereby provided.

name	T_{eff} (K)	$\log(g)$
star1	5669	4.40
star2	5527	3.44
star3	5734	3.17
star4	5325	3.01
star5	5448	3.36
star6	5617	3.59
star7	5414	3.26
star8	5410	3.28
star9	5337	3.05
star10	6281	4.48
star11	6175	4.47
star12	6687	4.29
star13	5301	3.38
star14	5338	3.29
star15	6628	2.92
star16	5592	3.58
star17	5410	3.28
star18	6188	4.46
star19	8894	4.25
star20	6389	3.99
star21	6469	4.32
star22	6456	4.40
star23	6307	4.55
star24	5281	2.98

Table 2.6: Stellar information taken from Gaia DR3: for every star the reference name, the effective temperature and the logarithm of the surface gravity are hereby provided.

Chapter 3

Synthetic spectra

The first step in the data analysis is the computation of synthetic spectra, which are required to identify the lines in the spectra and to determine the chemical abundances of the target stars. This requires a *model atmosphere*, which provides the temperature and gas pressure as a function of optical depth, thus tracing how these quantities vary from the outermost to the innermost layers of the stellar atmosphere. From a theoretical point of view, absorption lines arise from transitions between energy bound levels and their strength depends on how these levels are populated. To determine this, the Saha and Boltzmann equations must be solved for each existing transition and at each optical depth: the Boltzmann equation describes the excitation phenomenon and depends on temperature, abundances, and atomic data, while the Saha equation governs the ionization phenomenon and depends on temperature, pressure, abundances, and atomic data.

When computing a synthetic line profile, the process starts at the base of the photosphere, where the continuum photons are produced. The radiation field propagates through progressively cooler and more rarefied stellar layers toward the surface. The code generating the synthetic spectrum solves the Saha and Boltzmann equations for each layer of the atmosphere and for each wavelength. Each layer has a specific temperature and gas pressure (both provided by the model atmosphere), and the flux emerging from an inner layer serves as input for the next outer layer. At each wavelength, layers absorb a portion of the continuum flux according to the chemical composition, so that the emerging flux results from the combined effect of all the layers.

This kind of description is usually carried out in the assumption of local thermal equilibrium (LTE) which simplifies the computation of radiation field and of the level populations. In this framework, whenever dealing with a specific energetic transition, it is possible to assume that the energetic levels involved are the only energetic levels that characterise the atom. This picture is obviously far from reality where the other levels, not involved in the transition, can have an impact on the levels' population. Furthermore, in a more realistic treatment the existence of connections between the different energetic levels should be taken into account.

Although LTE is a simplifying assumption, it can still be used in the computation of the synthetic spectra. Indeed, there are only two conditions in which LTE assumption doesn't work properly: in extreme giant stars and in the outermost layers of the stellar atmosphere. In particular, extreme giant stars are characterised by very low surface gravity, very low effective temperature and very rarefied atmosphere, which by definition never verifies the condition of LTE. On the other hand, the most external layers of the

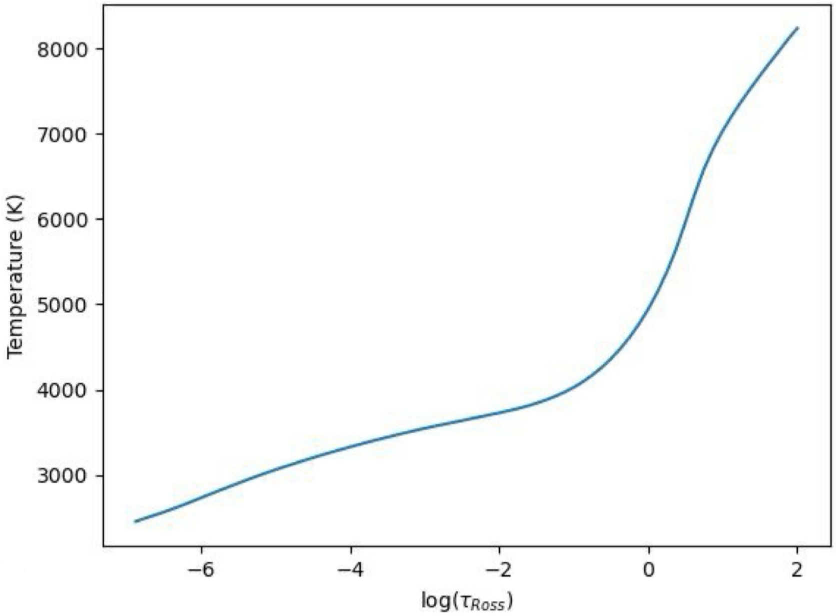

Figure 3.1: Example of the thermal structure of a model atmosphere, showing the behaviour of the temperature as a function of the optical depth.

stellar atmosphere are very rarefied and are also less physically known. Looking at the behaviour of the temperature as a function of the logarithm of the optical depth τ (see Fig.3.1), the innermost layers are characterised by a rather large temperature which, moving towards the outermost layers decreases first steeply and then more slowly. The coldest regions are also the most unknown ones not only because the conditions of LTE are not satisfied any more but also because correspondingly to the chromosphere there should be a slight increase of the temperature that in Fig.3.1 is not taken into account. The problem is that a detailed theoretical treatment of the chromosphere hasn't been proposed yet, so the only possibility is to proceed with a more empirical approach. The ignorance regarding the outermost regions could lead to think that the assumptions used are too rough, but in reality the majority of the lines that will be employed for the abundances computation are located approximately in the $\log(\tau) \in [-1, +1]$ region, which is much better understood and well reproduced even in the assumption of LTE.

The next fundamental step consists in understanding the line formation mechanism. Precisely, if the line is weak with respect to the continuum it means that the absorption provided by the atoms hasn't been significant so this line must have formed mainly in the innermost region of the stellar atmosphere, close to where the continuum emission is produced. If instead the line is strong, meaning that the absorption phenomenon has been quite significant, then it must have formed more outwards with respect to the formation region of weaker lines.

An important limitation of this description is given by the one-dimensional static model atmosphere with which the convection phenomenon is treated. To understand better the nature of this limitation we have to consider the curve of growth, which is given by the logarithm of the reduced equivalent width as a function of the logarithm of the number of active atoms (see Fig.3.2). Overlapping the observed curve

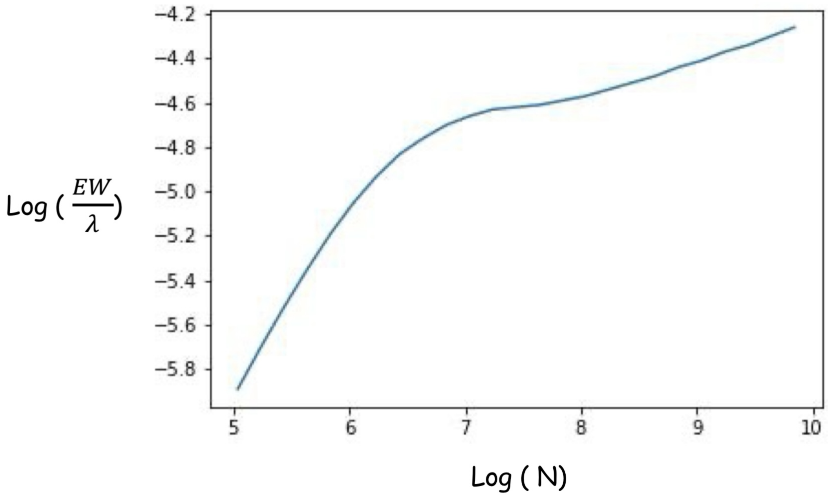

Figure 3.2: Curve of growth given by the reduced equivalent width represented as a function of the number of atoms providing the transition (both axis are in logarithmic scale).

of growth with the theoretical one, it is possible to notice that in the linear regime there is a perfect superposition of the two, while looking at the saturated region the observed points are well above the theoretical curve. This implies that the one-dimensional static model atmosphere predicts the line to be weaker than it really is, hence it is not realistic enough.

The reason behind this is that the formation mechanism for a weak line happens over one or two layers of the stellar atmosphere and since the convection happens on larger scales then the weak line doesn't feel significantly this effect. On the other hand, strong lines, meaning lines that have formed on larger scales, are more affected by the convection phenomenon and provide the aforementioned discrepancy between the observed and the theoretical curve of growth. This discrepancy can be solved by introducing the *microturbolent velocity* which is defined as a corrective parameter for which in the analysis a sum in quadrature between the Doppler velocity field, which is an isotropic Gaussian field, and this new term is performed. This implies that the microturbolent velocity is a free parameter that brings the observed curve of growth to match with the theoretical one even in the saturated region.

3.1 Computation of model atmosphere and synthetic spectra

The computation of both the model atmosphere and the synthetic spectra is carried out thanks to `k2`, which is a python code developed at the Department of Physics & Astronomy of the University of Bologna and devoted at calculate model atmospheres and synthetic spectra. The code manages the codes `ATLAS9` and `SYNTHE` (e.g. Castelli and Kurucz, 2003) that calculate model atmospheres and synthetic spectra, respectively. Below we describe the main parameters and information needed to perform these calculations.

3.1.1 The computation of the model atmosphere: `ATLAS9`

In this project the `ATLAS9` model atmosphere has been used (e.g. Castelli and Kurucz, 2003). `ATLAS9` employs the Opacity Distribution Function (ODF). These are tables including the absorption coefficient as a function of temperature, pressure and density and they are calculated for a fixed [M/H] and [α/Fe]. The advantage to use the ODF is to significantly speed up the calculation of a model atmosphere with the same [M/H] and [α/Fe] of the adopted ODF. Adopting the appropriate ODF, `ATLAS9` calculates the model atmosphere that is defined according to:

- `T` which is the effective temperature of the star;
- `logg` which is the logarithm of the surface gravity;
- `[M/H]` which is the metallicity of the adopted ODF;
- α which is the parameter that establishes the $[\alpha/Fe]$ value;
- v_t which is the microturbolent velocity expressed in km/s. The allowed values for `ATLAS9` are 0, 1, 2, 4, 8 km/s so if the value provided for v_t differs from these ones then the code skips the command and moves to the next one;
- `output` which is the name given to the model atmosphere obtained by using this command;
- $\mathtt{lg}\tau_{R0}$ which is the value of opacity for the outermost layer;
- $\delta\mathtt{lg}\tau_R$ which indicates what is the step in opacity between consecutive layers;
- N_{layers} which is the total number of layers;
- N_{iter} which is the number of blocks made of 15 iterations each for the computation of the model atmosphere.

3.1.2 The computation of the synthetic spectrum: `SYNTHE`

The synthetic spectra are calculated providing the appropriate model atmospheres (as specified above), the lists of atomic and molecular transitions available in the adopted spectral range and spectral resolution of the Gaussian profile to be convolved with the emergent spectra.

The first five input parameters are quite intuitive and they are simply: effective temperature, logarithm of the surface gravity, metallicity, $[\alpha/Fe]$ (which indicates how the α elements differ with respect to the prediction of the model atmosphere) and microturbolent velocity. They define the ODF used for the computation of the `ATLAS9` model atmosphere and in particular, knowing that v_t can have only specific values in the model atmosphere, for the value of microturbolent velocity provided by the user the code adopts the ODF characterised by the closest and smaller v_t to the one given as input. This means that if the input is for instance $1km/s < v_t < 2km/s$ then $v_t = 1$ km/s is the value adopted by the code for the production of the corresponding model atmosphere.

The input parameter `linelist` requested by `SYNTHE` is the name of an input file, which contains the full path of files setting the lists of lines, both atomic and molecular, that must be considered when computing the synthetic spectrum.
At this point the code is aware of all the energetic transitions in play and, knowing what happens in every layer of the stellar atmosphere from a thermodynamical point of view, it can proceed with the computation.

The next three input parameters for `SYNTHE` are once again quite intuitive: λ_1 and λ_2 terms identify the wavelength range over which the synthetic spectrum is computed, while the `R` defines a spectral resolution. This last term is relevant because up to now the code has computed a synthetic spectrum in which the lines representing the energetic transitions are only characterised by the so-called intrinsic broadening. The problem is that the observed spectrum is usually dominated by the instrumental broadening. Considering that the synthetic spectra are needed because a comparison with the observed spectra will provide the abundances of different elements, in order for this comparison to give reliable results the synthetic spectra must be characterised by a broadening similar to the observed one. This is the reason why once the synthetic spectrum is produced, it is immediately convolved with a Gaussian profile that has a full width at half maximum (FWHM) corresponding to the value of resolution given by `R`.

Finally, the `output` parameter indicates the name associated to the synthetic spectrum obtained.

3.2 Selection of lines

Our goal is to identify lines of different elements including only the isolated ones and those with a negligible level of contamination with close lines. We used the code `k2` to quantify the level of contamination of each transition. The keyword now employed in the input file is `sline` which stands for *selector of lines* and it requires four input parameters, namely `rootname`, `SNR`, `EWmin` and `nFWHM`.

The code analysed a previously computed synthetic spectrum and all the transition included in the calculation. All the minima of the synthetic spectrum are associated to the strongest transitions. For each of these lines, all the transitions within a window of `nFWHM` are considered (with `n`=1.4 in order to consider the main body of the line profile). Once the window has been selected, the code looks at all the energetic transitions (listed in the `.lin` file) that fall inside this specific range of wavelengths and identifies the strongest transition in terms of `EW`.
The problem that comes from dealing with a synthetic spectrum is that, by definition, it doesn't have noise. As a consequence of this, even a very weak line is still recognised by the code. From a practical point of view though, these weak lines are not visible and for this reason the user should give the keyword `SNR`, which in a normalised spectrum is $1/\sigma$ with σ being the standard deviation of the signal. `SNR`'s value coincides with the signal-to-noise ratio computed starting from the observed normalised spectrum and following the steps described in Sect.2.1.1. The idea is that the code takes as a threshold $1 - 3\sigma$ meaning that only lines deeper than this threshold are saved.
The output provides for each line corresponding to the minima of the spectrum the main information about the possible contamination with other lines together with the corresponding variation in abundances if the contamination is neglected. Additionally, the code identifies if a line is characterized by isotopic and/or hyperfine splitting, therefore whether it is contaminated by other lines but arising from same transition
The rule of thumb is to have a look at this `.linelist` file and ask for a trade off between saving a high number of lines for every element in order to have good statistics and preventing the inclusion of lines that are too contaminated. From a practical point of view, this means that it is necessary to keep only lines that are not contaminated or, if they are, to save only lines with `deltaAbu` < 0.1 so that the contamination is not too strong. At the end, we have identified a set of reliable and isolated lines for Fe, Mg, Na, Ti, Zn, Ni, Ca, Sc, Co and Ba.

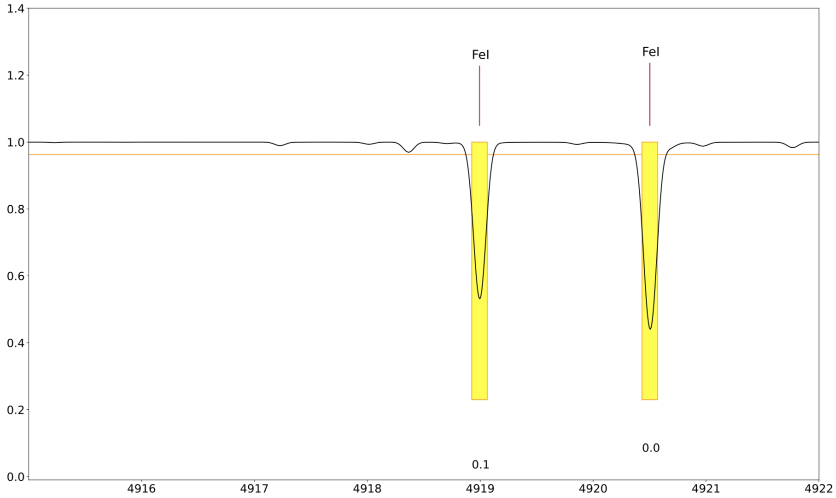

Figure 3.3: Example of the `.pdf` file obtained through `sline`. In black there's the synthetic spectrum, in orange the threshold $1 - 3\sigma$ previously mentioned, the window considered by the code is painted in yellow and for every line the code tells the user what is the corresponding element and ionisation state and the value corresponding to `deltaAbu`.

Chapter 4

Radial Velocities

4.1 `DAOSPEC`: radial velocities and chemical abundances of target stars

The radial velocity is defined as the velocity that the star has in its motion along the line of sight. In the case in which the star is moving closer to the observer, the lines in the spectrum, because of the Doppler shift, will be blue-shifted meaning that the observed wavelength (λ_{obs}) is smaller with respect to the rest frame one (λ_{rest}). Vice versa, if the star is moving away from the observer along the line of sight, then the lines in the spectrum will be redshifted so that $\lambda_{obs} > \lambda_{rest}$. This implies that it is possible to have a first estimate of the radial velocity using the formula that describes the Doppler shift:

$$\frac{\lambda_{obs} - \lambda_{rest}}{\lambda_{rest}} = \frac{RV}{c} \tag{4.1}$$

meaning that in order to obtain the radial velocity it is necessary to measure the distance between the observed and the rest-frame wavelength characterising a given spectral feature.

Radial velocities of the target stars were measured with the code `DAOSPEC` (e.g. Stetson and Pancino, 2008) that provides radial velocities and equivalent widths for metallic lines using a Gaussian fitting. For star19 where metallic lines are not visible and star15 showing problems in the radial velocity derived by `DAOSPEC`, we adopt the cross-correlation function method.

`DAOSPEC` is a code written in standard Fortran 77 that works with standard `fits` files and it was designed in order to work with high resolution spectra ($R > 15000$) and high signal-to-noise spectra ($SNR > 30$) that have been binned on a linear wavelength scale (see Stetson and Pancino, 2008).
The configuration parameters specify some basic information required by the code like for instance the wavelength limits of the spectral region of interest, a first guess for the FWHM and the order of the polynomial function used for the continuum normalisation. In particular, this last information highlights that in this spectral analysis, the technique used by the code to normalise the spectrum is different with respect to the median smoothing technique employed in the preliminary inspection of the given spectra (see Sect.2.1.1). The polynomial fitting technique is less sensitive to the presence of lines with respect to the median smoothing and basically provides a fit of the continuum level employing a Legendre polynomial.

The other two inputs have already been discussed in the description of this project. The spectrum is in this case in standard `fits` format, while the reference line-list contains the key information regarding the highest possible number of clean and unblended lines that characterise the wavelength range of interest.

Starting from these three inputs, the code performs a preliminary continuum fit using Legendre polynomials of the order specified by the user and it also performs the *line finding procedure*. Subsequently, the code correlates the detected lines with the ones listed in the line-list input file so that a first estimate of the radial velocity is provided. This is then the starting point of the main iteration loop.
The lines detected by the code are provisionally subtracted from the spectrum and the remaining residual spectrum is used to refine the continuum normalisation previously mentioned using robust non-linear least squares. At this point, with the newly normalised spectrum, the individual line centroids and strengths are refined, together with a value for the FWHM that can be either constant for all the considered lines or it can be a linear function of the wavelength. This procedure is then repeated five times, after which the fitted wavelengths of the individual lines are compared to the table of laboratory wavelengths. An outlier-clipping algorithm is then used to determine the final radial velocity estimate and also to indicate which of the detected lines lie sufficiently close to the tabulated laboratory wavelengths to be regarded as legitimate detections of specific atomic transitions.
The equivalent widths are computed from the fitted line parameters and the corresponding uncertainties are determined from the residual noise remaining in the spectrum within the wavelength range of the line profile.
The output of the code provides the estimate of both the FWHM and of the radial velocity with its standard error, the number of lines used in order to establish this radial velocity and the root mean square value of the pixel by pixel flux residuals remaining in the spectrum after the subtraction of all the fitted lines, expressed as a percentage of the continuum flux.

In order to manage automatically `DAOSPEC` for a large set of spectra, we used the wrapper `4dao` (e.g. Mucciarelli, 2013).

Even if in most cases the code is able to converge, providing the value of FWHM and order of the polynomial, in some others it will not be able to do this. When this happens, the FWHM must be fixed to the input value. To choose this, there are two possible strategies: either from the output pdf file, which contains several line plots, the user can determine what is a proper value for the FWHM or this could be fixed to the median or mean value among the ones obtained from a convergence. The main idea is that if the FWHM is fixed to a too high value it is as if the spectral resolution decreases; on the other hand, if the fixed value of the FWHM is too low the effect is the opposite. So the idea is that comparing the line produced by the code, which tries to fit in the best way possible the observed feature, and the observed line itself, it is possible to understand whether the input FWHM is correct or not. To understand this better from a visual point of view see Fig.4.1. Here on the left the FWHM, fixed to the input value, is too high and intuitively it is as if the spectral resolution has been reduced. In the central panel there is basically the opposite case, hence a too small FWHM, and finally on the right there's the case in which the value associated to the FWHM is the correct one. Thanks to these three examples it is possible to appreciate how a correct value of FWHM gives a configuration in which the line created by the code (in red) well reproduces the observed line (in black) which is exactly what is requested in this part of the analysis.

In the same way, also providing a meaningful value of the polynomial's order is of fundamental importance. Generally, a good value for the order of the Legendre polynomial necessary to normalise the spectrum is 5 if the input spectrum is already normalised and 8 in the case in which it isn't. The general rule is that a

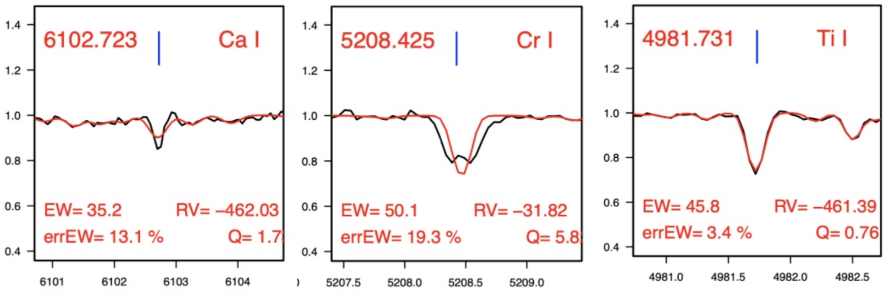

Figure 4.1: Some examples of fit performed by `DAOSPEC` on individual lines adopting too large or too low FWHM values (left and middle panels), and adopting the optimized FWHM (right panel).

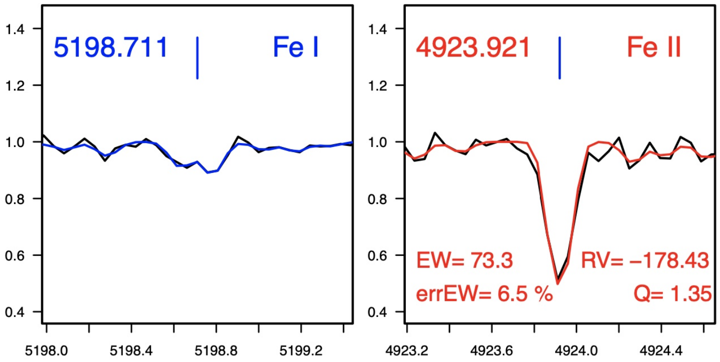

Figure 4.2: Examples of rejected and good lines fitted by `DAOSPEC` (left and right respectively).

relatively low order is not sensitive to the presence of lines. On the other hand, a large value of this order allows to reproduce in more details the variations of the continuum, sometimes also by reproducing the shape of the lines, which is exactly what we want to avoid here. In other words, the order of the Legendre polynomial must be such that only the behaviour of the continuum is reproduced by it.

quantity of interest	CD3	CD4	CD6	redl	redu
FWHM (guess)	2 pixels	3 pixels	4 pixels	8 pixels	8 pixels

Table 4.1: Guess values for the FWHM: these are the initial values for the FWHM that the user must insert in `4dao.list`.

The code provides in output a `pdf` file including for all the transitions provided in input the observed line and the best-fit. An example is shown in Fig.4.2. These plots are used to perform a visual inspection of the optimized FWHM and the degree of the polynomial function used for the normalization.
There are then other two output files: the normalised and corrected for radial velocity spectrum (`NZV` spectrum), which is very useful especially to perform additional chemical analysis through spectral synthesis technique (see Sect.5.3), and the `.in` file which contains all the main information about the equivalent

width measurements line by line. This file is then used as input for `GALA` in order to convert the equivalent widths in chemical abundances (see Sect.5.2).

4.2 Star19 and Star15 radial velocities: cross correlation technique

In the case of star19 and star15 (see Tab.2.3), the approach used by `DAOSPEC`/`4dao` (Gaussian fit of individual metallic lines) is not adequate because of the lack of metallic lines in their spectra. For these two stars we measure the radial velocity using the cross-correlation technique (see Tonry and Davis, 1979).

This technique uses the entire spectrum and computes the probability of having a good match between the observed spectrum, which must be shifted by a certain $\Delta\lambda$, and a template spectrum. This means that the first step in this technique is to choose a template spectrum which is a theoretical spectrum with a known radial velocity and similar features with respect to the observed one. In particular, it is better to choose the template with $RV = 0$ km/s so that the comparison between the observed and the template spectra provides directly the absolute value of the radial velocity. On the other hand, choosing a template spectrum with similar features to the observed one implies that the template spectrum must be of the same spectral type as the observed one, it must be characterised by a high SNR and a spectral resolution similar to the one characterising the observed spectrum.
Once the template spectrum is chosen, the observed spectrum must be shifted by $\Delta\lambda$ until there is a good match, hence an almost perfect superposition, between the observed spectrum that has been shifted and the template spectrum (see Fig.4.3). The cross correlation function that computes the probability of having this good match is defined as follows:

$$CCF = \sum_i Templ(\lambda_i) \times Obs(\lambda_i + \Delta) \tag{4.2}$$

so that by representing the cross correlation as a function of $\Delta\lambda$, the value of $\Delta\lambda$ that gives the maximum of CCF is the one from which the radial velocity is obtained.

The SNR and the spectral resolution both affect the cross correlation function. In particular, the SNR has an effect on the quality of the cross correlation function. This means that if we're dealing with a low SNR spectrum, then the position of the cross correlation function's peak won't change but the CCF will not reach the value of one so we obtain a low quality solution for the radial velocity. On the other hand, the spectral resolution is such that higher values of R provide a cross correlation function that is narrower so that a high precision and very accurate radial velocity can be obtained.

Using the cross correlation technique we have been able to compute the radial velocity for star19 (RV$= -66$ km/s) and to check the one provided for star15 by `4dao`.

4.3 A possible binary star

The target star1 shows some peculiarities in its spectrum, with the presence of some double features. Fig.4.4 shows an example of some double lines in the spectrum. One possible way to justify this characteristic is that probably this is a star belonging to a binary system. The problem with this kind of

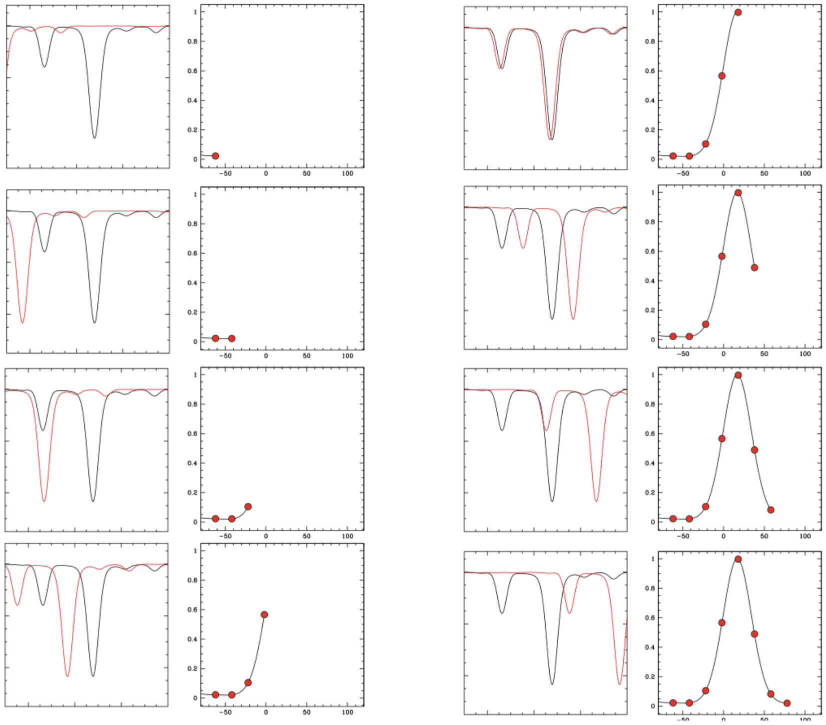

Figure 4.3: Sketch of how the cross correlation function is made. Step by step, by translating the observed spectrum of a certain $\Delta\lambda$ with respect to the theoretical one, the match between the two improves until it returns the best match correspondingly to the peak of the cross correlation function.

interpretation is that if it really is a binary star then the photometric information provided by Gaia are not reliable because, when observing a binary system, Gaia is not able to resolve its two components. Therefore the observed spectrum is the superposition of the two individual spectra. If the parameter `ruwe` provided by the Gaia DR3 archive is larger than 1.4 then this indicates problems with the astrometric solution that may be caused by binarity, but in this case `ruwe = 1.1148516` meaning that Gaia does not recognise this as a binary but the spectrum suggests otherwise. Since there is this inconsistency between what is observed in the spectrum, together with its most reasonable explanation, and the information provided by the Gaia DR3 archive, we have looked for other clues that could help us shed light on this issue. We noticed that not only the spectrum, but also the cross correlation function, whose shape should be a proxy also of the line's shape, presents two main peaks meaning that the "double feature" that we noticed in the spectrum is real (see Fig.4.5 for the shape of the cross correlation function where the two main peaks are pointed out by the arrows). Due to this uncertainty we have decided to extract this star from the sample and hence to pause its spectral analysis for the moment.

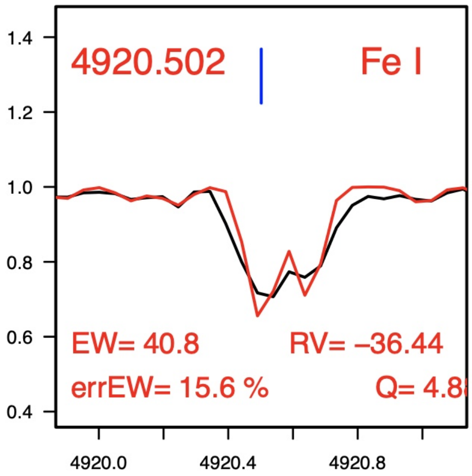

Figure 4.4: Example of the fit performed by `DAOSPEC` around a Fe line and where a second component is identified.

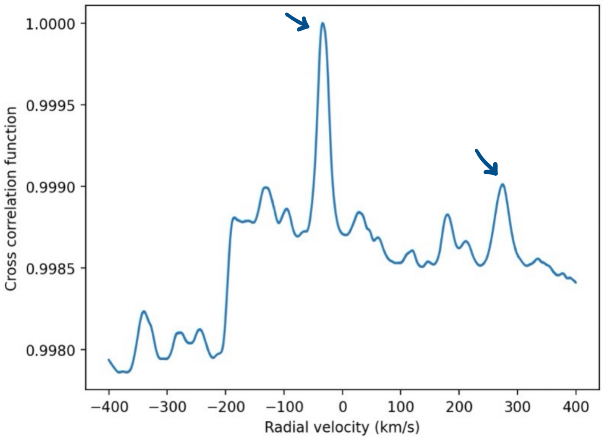

Figure 4.5: Cross correlation function for the target star1. It is possible to notice the existence of two main peaks, indicated by the arrows, surrounded by a high number of secondary peaks.

4.4 Radial velocities of ED-2 stars

Once the radial velocities have been obtained for all the stars in our sample (see Tab.4.2), we have verified the consistency of our results with the ones provided by the Gaia DR3 archive. To quantify the agreement between two values considering their respective uncertainties, we consider for each star the difference between the two radial velocities normalised to the sum in quadrature of the corresponding uncertainties:

$$\frac{\Delta_{RV}}{\sigma} = \frac{RV_1 - RV_2}{\sqrt{\sigma^2_{RV1} + \sigma^2_{RV2}}} \tag{4.3}$$

In this paragraph, we highlight both the normalized difference between the spectroscopic determination of radial velocities with the values provided by Gaia and the normalized difference between the spectroscopic estimates of radial velocities provided by the different channels used for the spectral analysis of the given stars.

Star	v_t (km/s)
star2	-43.27 ± 0.38
star3	-151.20 ± 0.80
star4	-461.40 ± 0.33
star5	-356.72 ± 0.33
star6	-372.33 ± 0.42
star7	-456.31 ± 0.35
star8	83.48 ± 0.78
star9	-178.50 ± 0.45
star10	-270.28 ± 0.80
star11	-383.71 ± 0.77
star12	-304.31 ± 1.57
star13	402.47 ± 0.18
star14	332.60 ± 0.20
star15	345.45 ± 0.19
star16	83.58 ± 0.17
star17	-277.40 ± 0.21
star18	83.66 ± 0.20
star19	-66.0 (CCF)
star20	66.72 ± 0.56
star21	62.76 ± 0.88
star22	-95.90 ± 0.66
star23	-351.12 ± 0.48
star24	304.75 ± 1.07

Table 4.2: For every star in our sample this table provides the values found by `4DAO` for the radial velocity.

Fig.4.6 shows the Δ_{RV}/σ as a function of the radial velocity measured in this study and colour-coded according to the G band magnitude and effective temperature.

Looking at these plots, it is possible to notice that all the points are within the $\pm 3\sigma$ range around zero so the spectroscopic determination of radial velocities has provided values which are consistent with the ones given by the Gaia DR3 archive. This is also the reason why in this project we haven't computed the orbits which instead have been computed in previous works such as the one by Ceccarelli et al., 2024 and Dodd et al., 2025: the proper motions are not varying with respect to the ones used in previous works and they coincide with the ones provided by the Gaia DR3 archive; in addition to this, the radial velocities computed in this work are fully consistent with those obtained by Gaia DR3 so we would obtain the same orbits as in previous works.

Another plot that is interesting to comment is the one in Fig.4.7 where only the stars with the CD3 and CD6 channels are represented and this provides the normalised difference between two spectroscopic determinations of radial velocities as a function of the radial velocity found from the CD3 channel coloured by the observed magnitude in the G band. All the data points fall practically within the range $\pm 1\sigma$ with

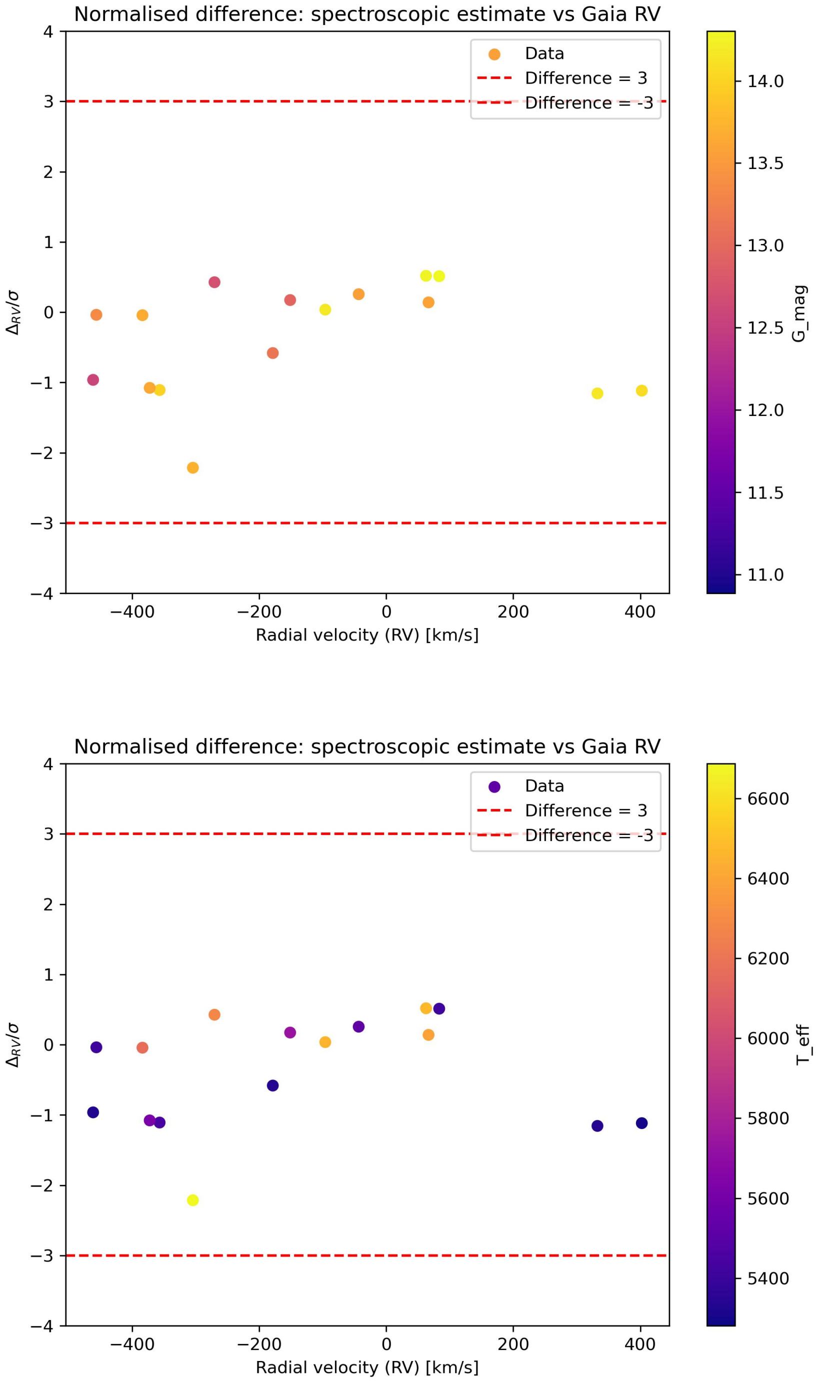

Figure 4.6: Radial velocity differences expressed in standard deviation units as a function of radial velocity, colour-coded according to G magnitudes (upper panel) and effective temperature (lower panel).

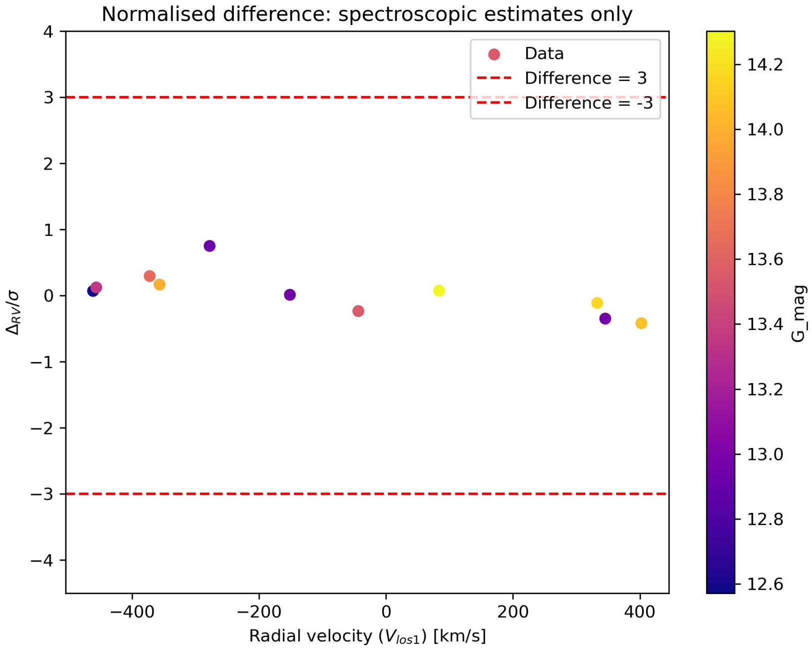

Figure 4.7: Radial velocity difference expressed in standard deviation units as a function of radial velocity, colour-coded according to G magnitudes only for stars with CD3 and CD6 spectral ranges.

respect to the value of zero. This result is due to the fact that the dispersion is coming, in this case, entirely by our analysis of the spectra, while in the previous plots it was coming both from our analysis and from the uncertainties provided by Gaia. Since the spectra that we dealt with are characterised by a similar quality and have all been taken almost simultaneously, it makes sense that in Fig.4.7 the dispersion is smaller with respect to the case of Fig.4.6.

Chapter 5

Chemical Abundances

The chemical abundances have been computed for all the stars except star1 (possible binary star, see Sect.4.3) and star19 (the hottest star in our sample see Sect.2.5.1) using two techniques, namely equivalent width (with the code `GALA`) and spectral synthesis (with the code `SALVADOR`), depending on whether the spectral lines are linear and isolated or damped respectively.

5.1 Determination of the chemical abundances: equivalent width technique

Generally, there are two possible methods that can be used in order to derive the chemical abundances of different elements, namely the spectral synthesis technique and the equivalent width method. Both of these methods are based on a comparison between the observed and the synthetic spectrum so that the best match between the two provides the chemical abundances of interest, still they present some differences.

The equivalent width (EW) is defined as the width, in wavelength units, of a rectangle characterised by a height of I_C, in intensity units, that has the same area as the absorption line. As a reference, it is possible to use Fig.5.1, where I_C is the level of the continuum and I_0 is the specific flux at the line center λ_0 measured upward from zero. The equivalent width represents basically the strength of an absorption line and it is computed as follows:

$$EW = \Delta\lambda \sum_i \frac{I_{Ci} - I_i}{I_{Ci}} \tag{5.1}$$

where $\Delta\lambda$ is the constant pixel size, I_{Ci} is the level of the continuum at the wavelength corresponding to the i-th pixel and I_i is the flux received by that same pixel. When dealing with real spectra though, the effects of noise, spectral defects and neighbouring lines can alter the profile of the absorption line. As a direct consequence of this, the EW cannot be computed using Eq.5.1. So, instead of a direct numerical summation, a numerical fit of a Gaussian-shaped function $g(\lambda)$ is employed and the equivalent width becomes:

$$EW = \int g(\lambda)\lambda \tag{5.2}$$

Knowing that a measurement has a physical meaning only if it also has an uncertainty associated to it,

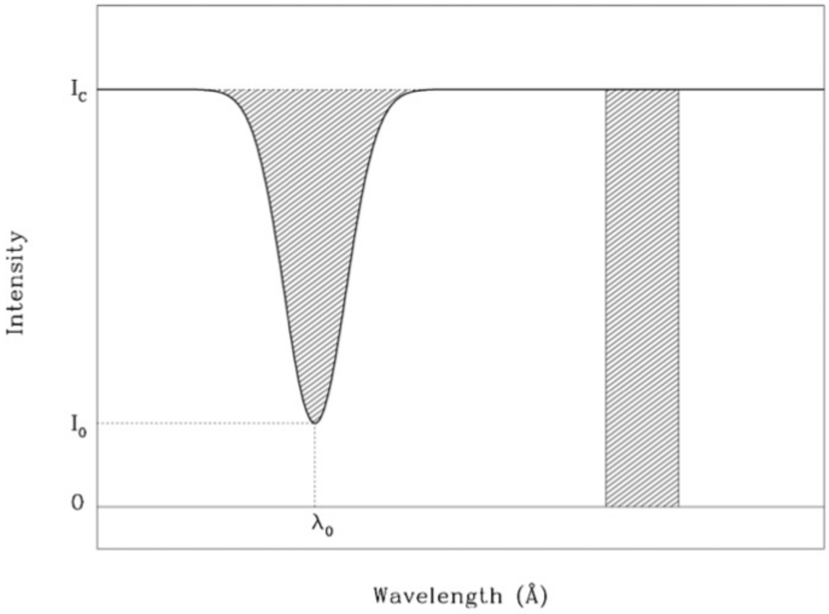

Figure 5.1: Representation of the classical definition of equivalent width (EW): on the *left* there's the actual absorption line for which the EW must be measured and on the *right* there's the rectangle with area equal to the one provided by the absorption line.

it is necessary also to provide a formula for such error. A way to compute this was provided by Cayrel in 1988:

$$\delta EW \approx 1.5\frac{\sqrt{\Delta\lambda \cdot FWHM}}{SNR} \approx 1.6\frac{\sqrt{\Delta\lambda \cdot EW}}{SNR} \tag{5.3}$$

where the uncertainty associated to the equivalent width depends on the SNR and on the FWHM of the line. This was just a first expression for the computation of the uncertainty associated to the EW which was then found to be only a lower limit for it because, formally, the true continuum level is not perfectly known since it has its own uncertainty that should be propagated through the computation. As a matter of fact, in order to take into account the uncertainty associated to the continuum, the derivative of Eq.5.1 should be computed both with respect to I_i and to I_{Ci} so that δEW becomes:

$$\delta EW = \sqrt{\left(\sum_i (\delta I_i)^2 \frac{\partial EW}{\partial I_i}\right)^2 + \left(\sum_i (\delta I_{Ci})^2 \frac{\partial EW}{\partial I_{Ci}}\right)^2} \tag{5.4}$$

where δI_i and δI_{Ci} are the uncertainties on I_i and I_{Ci} respectively.

The idea at the basis of the equivalent width technique then is to compare the flux provided by an observed absorption line and the one predicted by the synthetic spectrum. This technique has both advantages and disadvantages. The most important advantage of this technique is that it is very rapid hence it allows to obtain the chemical abundances in a relatively short period of time. On the other hand, one of the main disadvantages of this technique is that it cannot be applied in several cases like in the presence of *damped lines*, meaning those that are characterised by a line profile which is not Gaussian.

Another case in which the EW technique cannot be used is the case of blending, since the contribution of different elements to the same feature cannot be properly disentangled, leading to erroneous abundance estimates. This implies that the hyperfine structures and the energetic transitions provided by the isotopes must be necessarily analysed with the spectral synthesis technique. The reason why the equivalent width technique works exclusively for unblended features is that the program which computes the equivalent width of every line does so by computing the synthetic spectrum only in the proximity of the given spectral line, so it is not able to treat multiple components. Finally, also in the case of *blanketing* the EW technique cannot be applied. This is a peculiar case in which the level of the continuum in the normalised spectrum is not located at 1, but it is slightly below this value. The reason behind this is simply that what appears to be the continuum is actually characterised by the presence of a high number of small absorption features which decrease the level of the continuum providing a value smaller than 1.

The EW method has been used in this work for Fe lines because for this element there is a large number of isolated and linear transitions. The EWs have been measured using the code `DAOSPEC` (see Sect.4.1) that provides the EW for each line for which also the radial velocity is measured. For every line the measured EW was translated in the corresponding chemical abundance using the code `GALA`.

5.2 Equivalent width technique: `GALA`

`GALA` (see Mucciarelli et al., 2013) is a code, written in standard Fortran 77, that allows to automatically derive some of the atmospheric parameters (effective temperature, surface gravity, microturbolent velocity and metallicity) and the abundances for individual species of stellar spectra using the method based on equivalent widths of metallic lines. In particular, `GALA` is designed to obtain the best model atmosphere by optimizing the four atmospheric parameters previously mentioned after rejecting the discrepant lines. In addition to this, by using the `WIDTH9` code developed by R. L. Kurucz (see Kurucz, 1993), it is able both to infer the abundances of individual and unblended spectral lines and to provide statistical and graphical tools to evaluate the quality of the final solution together with the uncertainty of the derived parameters. In order to obtain the chemical abundances for different elements, the code compares the measured equivalent widths, which are provided as output by `4dao`, with the theoretical strength of the line, changing the abundance until the observed and the theoretical equivalent widths match within a convergence range.

`GALA` is structured in three main working blocks:

- the *guess* working block which finds the guessed atmospheric parameters in a fast way;
- the *analysis* working block which finds the best model atmosphere through a local minimization starting with the guessed parameters obtained from the previous working block;
- the *refinement* working block which refines the solution, starting from the atmospheric parameters obtained from the previous working block.

First, we ran GALA fixing T_{eff} and $\log g$ to the photometric values obtained from Gaia DR3 photometry (see Sect.2.2). Starting at the first run the metallicity of the model equal to -2.44 dex (according to Dodd et al., 2025) we optimized the microturbolent velocity, the only free parameter characterizing the photospheres. Because of the relatively low number of Fe I lines (≈20 lines) available for the dwarf targets, the optimization of the microturbolent velocities results to be very uncertain, with an impact on the derived abundances. For this reason, we decided to use for all the dwarf stars of ED-2 the median value of the microturbolent velocities obtained by Ceccarelli et al., 2024 for stars in a similar evolutionary

stage. To be more precise, what we did was to plot the Kiel's diagram (see Fig.5.3) representing both the stars analysed by Ceccarelli et al., 2024 and the stars analysed in this work in blue and pink respectively. Then we considered the dwarf stars in the work of Ceccarelli et al., 2024 that share similar T_{eff} and $\log(g)$ to our dwarf stars and by looking at their results we have assumed that the mean v_t value found by Ceccarelli et al., 2024 for these stars was the right value for our dwarf stars. This has brought to a final run of `GALA` where the microturbolent velocity is optimized in the case of giant stars while it is fixed to the input value of 0.9 km/s (the one found with this comparison) in the case of dwarf stars.
On the other hand, for giant stars this parameter is well constrained thanks to the large number of available Fe lines, so we adopted the value provided by `GALA`. Table 5.1 shows the microturbolent velocities obtained for all the target stars in our sample.

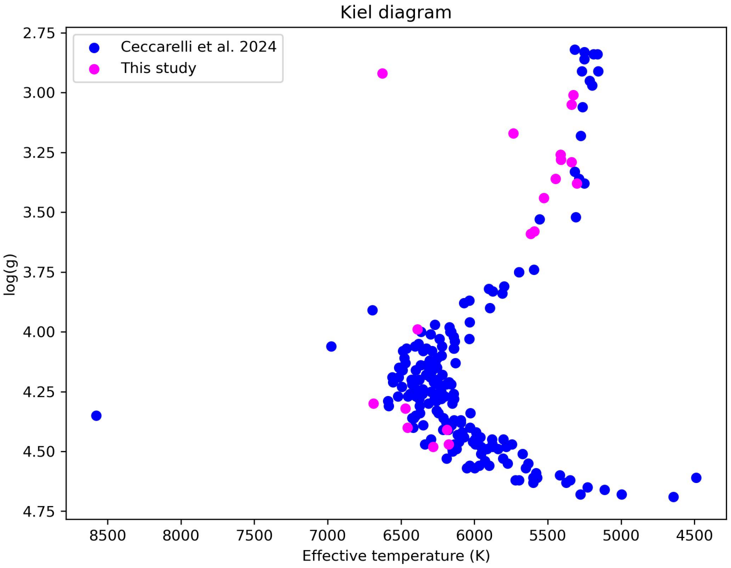

Figure 5.2: Position in the Kiel diagram of the targets of Ceccarelli et al., 2024 (blue points) with superimposed the targets of ED-2 of this study (magenta points).

Star	v_t (km/s)
star2	1.70
star3	1.80
star4	1.30
star5	1.60
star6	1.40
star7	1.60
star8	1.00
star9	1.10
star10	0.90
star11	0.90
star12	0.90
star13	1.50
star14	1.60
star15	1.80
star16	1.40
star17	1.80
star18	0.90
star20	0.90
star21	0.90
star22	0.90
star23	0.90
star24	1.70

Table 5.1: For every star in our sample this table provides the values found by `GALA` for the microturbolent velocity.

5.3 Determination of the chemical abundances: spectral synthesis technique

In case of complex transitions (affected by damped wings, blending or splitting) the EW method cannot be used and it is better to compare the observed profiles with synthetic spectra. The code employed for this procedure is `SALVADOR` (Alvarez Garay et al. in prep) that performs a chi-square minimization between the observed profile and a grid of synthetic spectra calculated with `SYNTHE` (see Sect.3.1.2) and assuming different abundances for the species of interest.
The first input file that this code needs for the comparison with the synthetic spectra is the normalized and corrected for radial velocity spectrum (sometimes indicated as NZV spectrum), which is one of the outputs provided by `4dao`. The normalization applied to the original observed spectrum is a global normalization; however, a local normalization might be needed for the correct application of the spectral synthesis technique. To perform the local normalisation, we need the continuum windows, hence ranges in wavelength where the spectrum is only characterised by a continuum emission, in order to match the level of the observed continuum with the one of the synthetic spectra.
Lastly, we also provide the spectral resolution of a Gaussian that must be convolved with the intrinsic spectrum in order to simulate the observed broadening of the line, which is dominated by the instrumental broadening as discussed in the third chapter.

Starting from the observed spectrum, for all the lines provided as input, `salvador` computes the synthetic spectrum using the appropriate stellar parameters of the target and looks at the difference between the observed and the synthetic spectrum. At this point, the code computes a set of synthetic spectra by changing exclusively the abundance of the element of interest and it does so until it computes the synthetic spectrum that provides the best match (through a χ^2 minimization) with the observed one.

Salvador gives three output files for every input spectrum. In the first output the user can evaluate, for every transition analysed through the spectral synthesis technique, the superposition between the observed spectrum in black and the set of synthetic spectra (all with different abundances for the element of interest). In addition to this, inside of the graphical window (see Fig.5.3) also the continuum windows are highlighted in yellow. This file also contains a zoom of the best fit of the line (see top right panel of Fig.5.3) and a plot representing the χ^2 as a function of the absolute abundance for the element of interest (see bottom right panel of Fig.5.3) so that the abundance returned by the code is the one providing the minimum χ^2.

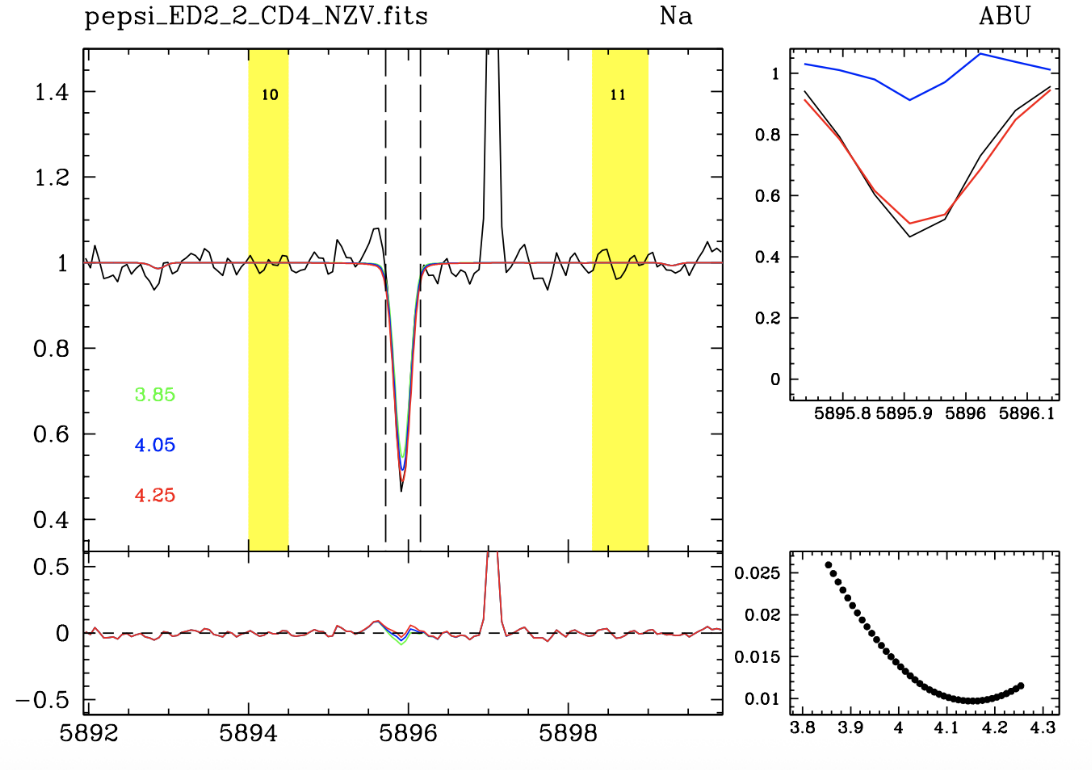

Figure 5.3: Example of the graphical output provided by `salvador`.

The final absolute abundances and a summary of the χ^2 minimisation are provided instead by the `.fit` and `.best` output files respectively.

Considering what has been just said regarding both the codes used to derive the chemical abundances and the problems related to the spectrum of star19, the [Fe/H] abundance (hence metallicity) cannot be established precisely. Because of the lack of visible lines, we derived upper limits for the Fe abundance. To do this, we have computed several synthetic spectra with $[Fe/H] \in \{-3, -2.44, -2, -1.5\}$ dex and we have plotted them over the observed spectrum (see Fig.5.4). The idea was to compare the synthetic spectrum with the observed one correspondingly to a line that is expected to be strong: from this comparison the upper limit that has been found is $[Fe/H] < -2$ dex for this star, which is consistent with the result obtained for all the other stars in this sample.

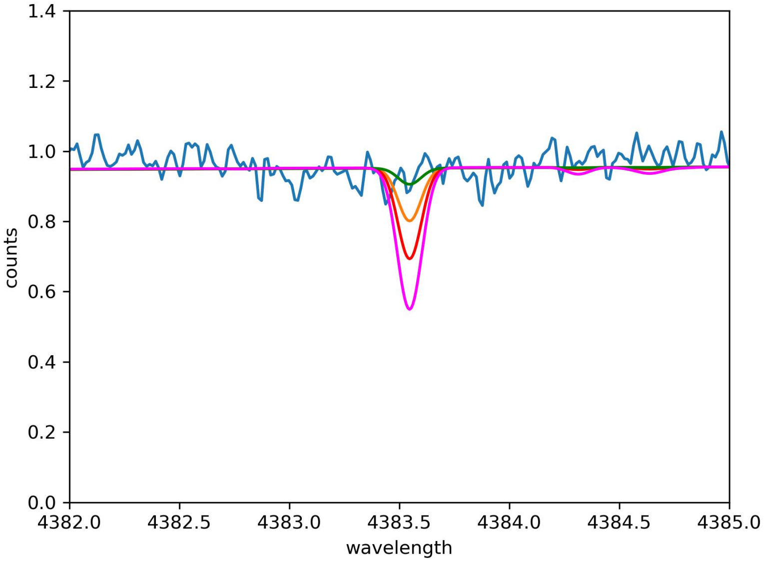

Figure 5.4: Comparison between the observed spectrum (in blue) and a set of synthetic spectra used in order to provide at least an upper limit for the metallicity of star19. In green is the synthetic spectrum with [Fe/H] = −3 dex, in orange is the synthetic spectrum with [Fe/H] = −2.44 dex, in red is the synthetic spectrum with [Fe/H] = −2 dex, in pink is the synthetic spectrum with [Fe/H] = −1.5 dex.

5.4 Computation of the uncertainties associated to [Fe/H] and to [X/Fe]

The total uncertainty in [Fe/H] ($\sigma_{[Fe/H]}$) is defined as the sum in quadrature of the error associated to the measurement of the Fe abundance and the errors due to the stellar parameters used:

$$\sigma_{[Fe/H]} = \sqrt{\frac{\sigma_{Fe}^2}{N_{Fe}} + (\delta_{Fe}^{T_{eff}})^2 + (\delta_{Fe}^{\log g})^2 + (\delta_{Fe}^{v_t})^2} \tag{5.5}$$

where σ_{Fe} is the standard deviation associated to the measurement of [Fe/H] in one star using a certain number of lines provided by N_{Fe} so that the error associated to the measurement is simply the error on the mean $\sigma/\sqrt{N}$. The quantities δ^{X}_{Fe} are telling us how much the abundance of Fe changes by using the quantity $X + \delta X$, instead of the stellar parameter X ($T_{eff}, \log g$ or v_t). In order to calculate the net abundance variations due to parameter variations, we assume typical uncertainties of 100 K in T_{eff}, 0.1 in $\log g$, and 0.2-0.4 km/s (for giant and dwarf stars respectively) in v_t, as explained in Sect.2.3.1.

For what instead concerns the uncertainties associated to the abundance ratios in the form [X/Fe], these have been computed through the following equation:

$$\sigma_{[X/Fe]} = \sqrt{\left(\frac{\sigma_{Fe}}{\sqrt{N_{Fe}}}\right)^2 + \left(\frac{\sigma_X}{\sqrt{N_X}}\right)^2 + \delta^2_{[X/Fe]}} \tag{5.6}$$

so that the final error for [X/Fe] is expressed as the sum in quadrature of the statistical error on the average value of [Fe/H], the statistical error on the average value of [X/H] and the variation of [X/Fe] due to the variation of the parameters.

5.5 MDF of ED-2 stars

The MDF can be used to understand whether ED-2 was originally a globular cluster or a more complex system like a dwarf galaxy. In particular, we are interested to investigate the metallicity spread of the ED-2 stellar sample in order to unveil if the observed spread is compatible or not with a null intrinsic spread that would imply a globular cluster nature of this system's progenitor.
According to their CMD and the uniqueness of their turn-off regions, any globular cluster includes stars formed in one single burst of star formation. These stars formed simultaneously from the same giant molecular cloud and as such they should have all the same chemical composition (or at least all the same [Fe/H]) and they should be of the same age. Focusing on the chemical characteristics of globular clusters, this implies that the metallicity distribution function is characterised by a null intrinsic scatter (e.g. Gratton et al., 2004, Carretta et al., 2009, Bastian and Lardo, 2018), meaning that the scatter seen in the MDF can be entirely explained with the uncertainties that characterise the chemical analysis and it is not due to an actual difference in the [Fe/H] values obtained for all the stars in our sample.
On the other hand, in more complex stellar systems (like dwarf galaxies) the stars formed in multiple burst of star formation, and the ejecta of supernovae are retained, therefore younger stars are more metal-rich (e.g. Tolstoy et al., 2009). This means that in the case of a dwarf galaxy the intrinsic scatter σ_{intr} is expected to be different from zero, so the values of [Fe/H] are intrinsically different among the stars in this kind of system.

`GALA` provides the value of [Fe/H] for all the stars in our sample with the corresponding errors, so that the MDF obtained can be appreciated in Fig.5.5 where the mean value of metallicity is [Fe/H]$= -2.33$ dex while the observed dispersion is $\sigma_{obs} = 0.13$ dex.

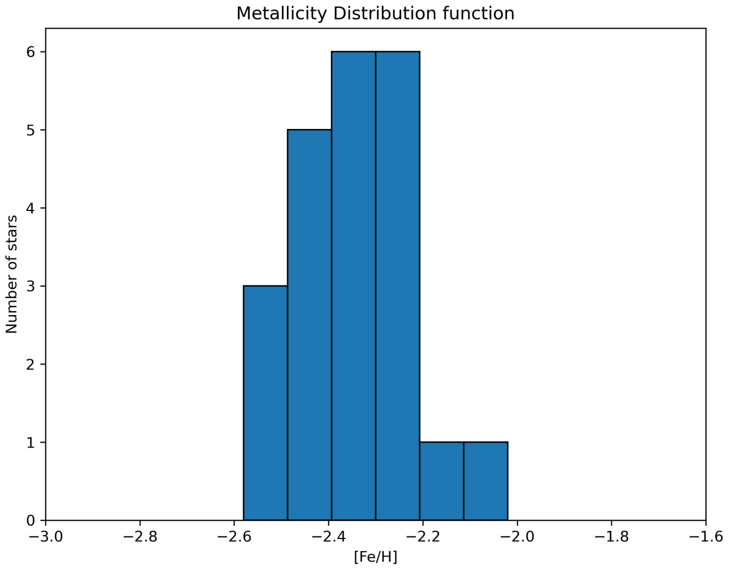

Figure 5.5: MDF of the entire sample of ED-2 stars. This provides a mean [Fe/H] of -2.33 dex and a standard deviation of 0.13 dex.

5.6 MCMC approach

In order to understand what is the specific case for ED-2 stars, we have used the Markov Chain Monte Carlo (MCMC) approach based on the *maximum likelihood principle*. This states that the parameters (in this case mean value of metallicity μ and intrinsic scatter σ_{int}) which maximise the likelihood function are those defining a model that best fits the given data (in this case the MDF for our sample of stars).

The Markov Chain Monte Carlo is a family of algorithms used to sample probability distribution functions. The term *Monte Carlo* is due to the fact that the sampling is random, while the term *Markov Chain* highlights how this is a stochastic process where the probability of the next state depends exclusively on the present state. The basic idea is that the starting point here is not provided by a random (μ, σ_{int}) combination, but it is provided by a guess value. Then, the code moves randomly in the (μ, σ_{int}) space and it tends to cluster in a region that returns the highest probability which corresponds to the region that has been crossed the highest number of times by the code.
Intuitively in this approach, which aims to find the (μ, σ_{int}) that reproduces the MDF, the first thing to do is to build a Markov chain that has as stationary distribution the target distribution. Then the chain is simulated for a high number of steps and after an initial phase, known as *burn-in*, the samples that have been generated are considered as representative of the target distribution. To do this, the so called *walkers* are needed. They are defined as virtual entities that explore the parameter space looking for the regions in which the likelihood function assumes the highest values, so the regions of highest probability. Usually, using a large number of walkers (here 250 walkers have been used) improves the estimate of the parameters and guarantees a convergence of the method. These walkers are independent one from the

name	[Fe/H] (dex)
star2	-2.24±0.08
star3	-2.58±0.08
star4	-2.24±0.08
star5	-2.25±0.08
star6	-2.31±0.08
star7	-2.28±0.07
star8	-2.22±0.08
star9	-2.32±0.08
star10	-2.40±0.09
star11	-2.38±0.20
star12	-2.42±0.11
star13	-2.51±0.11
star14	-2.41±0.10
star15	-2.53±0.56
star16	-2.45±0.10
star17	-2.34±0.08
star18	-2.10±0.33
star20	-2.40±0.09
star21	-2.32±0.08
star22	-2.02±0.11
star23	-2.28±0.18
star24	-2.37±0.30

Table 5.2: Measures for the [Fe/H] abundance of our target stars.

other but they still influence each other when proposing the next step.
Starting from a guess value in the parameter space, every walker proposes a new position, which is accepted or rejected on the basis of relative probability. As a matter of fact, in the MCMC sampling, it is not necessary to know the absolute value of the probability distribution; only the ratio between the probabilities of two points is needed. So every time that a walker proposes a new point, the MCMC sampler computes the ratio between the likelihood function in the new point and the likelihood function in the old one. If this ratio gives a value larger than or equal to one then this new point is accepted and the walker goes to it, otherwise it doesn't. This procedure is repeated several times building up a chain that follows the distribution of interest.

5.7 Intrinsic [Fe/H] scatter in ED-2

Using the MCMC approach previously described, we derive a mean value of [Fe/H] of -2.33 ± 0.03 with an intrinsic scatter of 0.096 ± 0.024 (see Fig.5.6). The derived intrinsic scatter naturally takes into account the uncertainties in [Fe/H] for each individual target. At this point, we started making a few considerations regarding our sample to understand whether this result was correct or if we were still missing something that could bring us to a result consistent with previous works.

By a visual inspection of the position of the targets on the Kiel's diagram (see Fig.2.6), we noted that

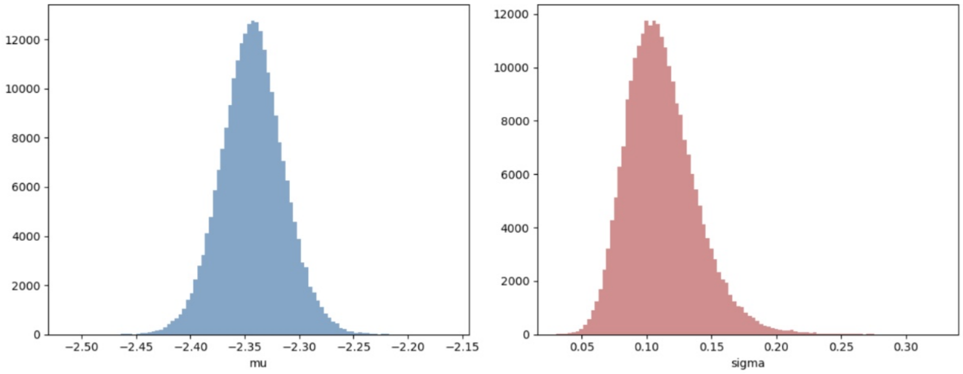

Figure 5.6: On the left is the distribution of the mean value of metallicity μ while on the right is the distribution of the intrinsic scatter σ_{int} both found thanks to the MCMC approach.

all the stars are compatible with a single isochrone but two, namely star3 and star15 (see Tab.2.3), that do not fall exactly on the isochrone which best fits all the other stars. This result has brought us to study the metallicity distribution function only for the stars that were fitted by the isochrone (see Fig.5.7).

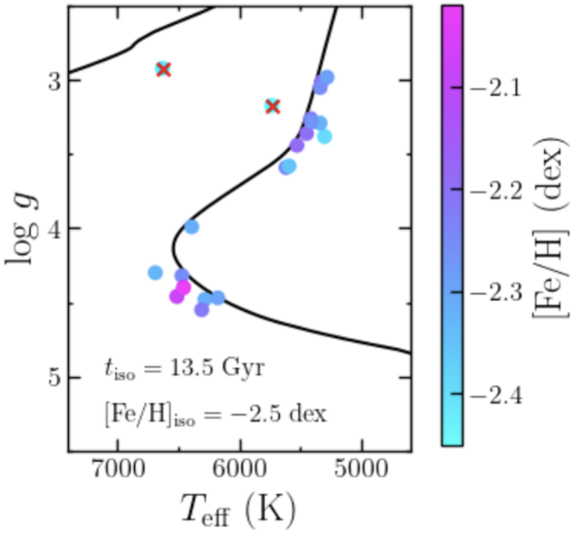

Figure 5.7: Kiel's diagram: data points coloured by the [Fe/H] abundance that was found with `GALA`. The red crosses represent the stars outside of the isochrone for which chemical abundances were derived anyway.

This selection leads to the MDF shown in Fig.5.8. The first result is that the mean value of metallicity that has been obtained is [Fe/H]$= -2.33 \pm 0.01$ dex, which is perfectly consistent with the results obtained from previous works. More importantly, there is the result displayed by the corner plot in Fig.5.8, according to which the intrinsic scatter is $\sigma_{int} = 0.04^{+0.04}_{-0.03}$. This is the result of the MCMC approach applied to the sample of stars fitted by the isochrone: it is possible to notice that the intrinsic scatter is consistent with zero. This, as explained before, indicates that the different values of [Fe/H] that have been found during the analysis are not due to an actual difference in the Fe abundance in these stars, but the scatter in the MDF is simply due to all the uncertainties that affect our analysis. This result supports the scenario where the progenitor of ED-2 was likely a globular cluster, because the lack of intrinsic [Fe/H] scatter suggests that the progenitor was not able to retain the ejecta of supernovae.

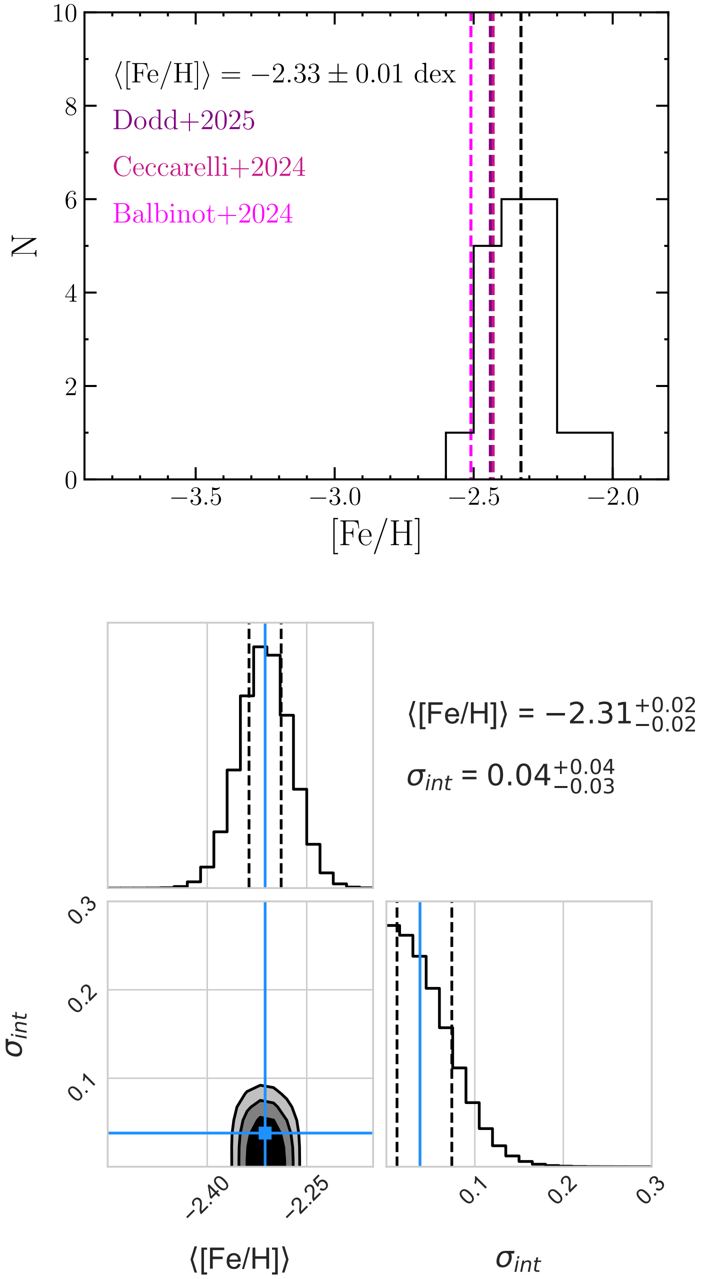

Figure 5.8: *Upper panel*: MDF of the ED-2 stars of this study, compared with the available values obtained from Balbinot et al., 2023, Ceccarelli et al., 2024 and Dodd et al., 2025. *Bottom panel*: corner plot that represents both the MDF of the ED-2 stars and the intrinsic scatter, which is found to be consistent with zero.

5.7.1 ED-2: MDF literature results

To sustain that our result is consistent with the ones found in previous works, we can remind that ED-2 is a stellar system that has already been studied by Balbinot et al., 2023, by Ceccarelli et al., 2024 and by Dodd et al., 2025. All these previous works have tried to use the metallicity distribution function in order to understand whether ED-2 was originally a globular cluster or a dwarf galaxy.
Previous studies are based on small samples of stars or on low/medium resolution spectra. Balbinot et al., 2023 has provided first a photometric characterisation of this specific stellar system using 48 member stars. From this kind of analysis he found that the isochrone best fitting the data was the one characterised by $\log(age/yr) = 10.20$ and [Fe/H]= -2.60 dex. The authors then realised that only 22 out of the 48 member stars were bright enough to allow the spectroscopic follow up, which was carried out through low and medium resolution spectra obtained thanks to LAMOST DR8 and APOGEE DR17. For what instead concerns Ceccarelli et al., 2024 and Dodd et al., 2025 the spectra have been taken with UVES and PEPSI, like in our case, but these works considered only 4 and 5 stars respectively. The results that they obtained for the metallicity distribution of ED-2 stars has already been anticipated in the introduction (see Fig.1.7): all three works have found a narrow metallicity distribution function centered at very metal poor values, which seemed to suggest that ED-2 stars have been accreted onto the Milky Way from a globular cluster.
Specifically, Balbinot et al., 2023 found [Fe/H]= $-2.60^{+0.20}_{-0.21}$ dex, Ceccarelli et al., 2024 found [Fe/H]= -2.43 ± 0.04 dex and Dodd et al., 2025 found [Fe/H]= -2.44 ± 0.06 dex which are all consistent with the value that we have found. In these works there is no detailed treatment of the intrinsic scatter probably due to the fact that the samples of target stars used are too small.

5.8 Lighter elements abundances of other elements

Apart from the MDF, providing the most striking difference to distinguish between a globular cluster and a dwarf galaxy, there are other quantities that can be used to distinguish between these two kinds of stellar systems. Focusing still on chemical abundances, a spread in the abundance of lighter elements such as Na and O is notoriously known as defining a stellar system as a globular cluster (see Carretta et al., 2009Bastian and Lardo, 2018 and Bastian and Lardo, 2018). In fact, the stars of a globular cluster formed by the same burst of star formation, hence should have all the same chemical composition, in reality by looking at the light elements abundances such as C, N, O, Na, Mg and Al there are strong evidences of both a spread in their abundances and of characteristic anti-correlations such as the O-Na, the Mg-Al and the Mg-Si ones so that for instance stars belonging to a globular cluster are either O rich and Na poor or the opposite configuration.

In particular, all the chemical anomalies that are observed in globular clusters concern elements that are produced during the hot H burning process, meaning in the CNO cycle. This is a thermonuclear reaction that converts four H^1 into one He^4 following the sketch represented in Fig.5.9.
The CNO cycle though also has secondary chains that can be triggered when the N^{15} captures a proton but, instead of producing $C^{12} + He^4$, it returns oxygen. The new proton capture that is triggered in this way provides the O-Na anti-correlation that was previously mentioned. Then, additional proton captures could bring to the formation of Mg and Al which are involved in other anti-correlations that are observed in globular clusters.
The problem is given by the fact that those processes can happen only if the temperature in the stellar interior reaches values above 2×10^7 K and the anti-correlations produced by those reactions are visible through the stellar spectra only in the presence of mixing processes that bring those by-products to the

stellar surface. According to this last consideration, the chemical anomalies should be visible only in RGB stars, but in reality they can be appreciated also in main sequence (MS) stars where the mixing processes are not active yet, meaning that these chemical anomalies must be primordial. The other reason that can be used to justify this intuition is that the temperatures needed in the interior of stars to produce such anomalies are never reached by the low mass stars that characterise the present day globular clusters in the Milky Way. For these anomalies to be primordial there is the need of a previous generation of stars, which are not shining any more, characterised by a mass significantly higher than the current stellar mass so that they could reach the high temperatures needed in the interior of the star to trigger the thermonuclear reactions producing these chemical anomalies and anti-correlations. According to this picture, the new generation of stars has been formed from a medium that has been polluted by the ejecta of the previous generation of stars.
The polluters, meaning the stars that could have been responsible for the anti-correlations, must be stars that don't explode like SN because otherwise the Fe abundance wouldn't be homogeneous in globular clusters. For this reason, AGB stars have been proposed as polluters, but this is still an open question.

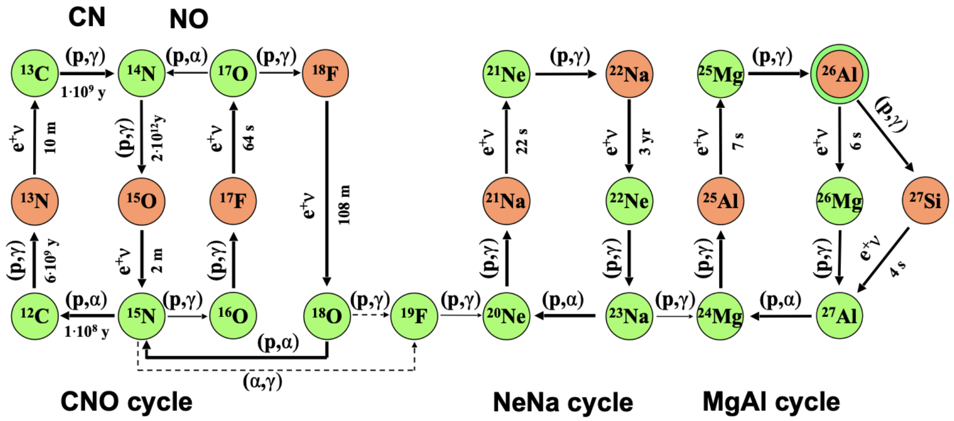

Figure 5.9: Sketch representing what happens during the CNO cycle (e.g. Boeltzig et al., 2016).

In this study we measured abundances for the α element Ca and the light elements Na and Mg. Calcium is a tracer of [α/Fe] while magnesium and sodium are particularly relevant because they give rise, in globular clusters, to anti-correlations so the presence of a significant spread in their abundances could flag the existence of these anti-correlation hence verifying the globular cluster nature of ED-2's progenitor. The results concerning these three elements can be appreciated in Fig.5.10. In particular, [Ca/Fe] provides an average abundance of 0.32 dex with an observed scatter fully compatible with a null spread. The derived abundances is consistent with the [α/Fe] observed in Milky Way stars of similar metallicities.

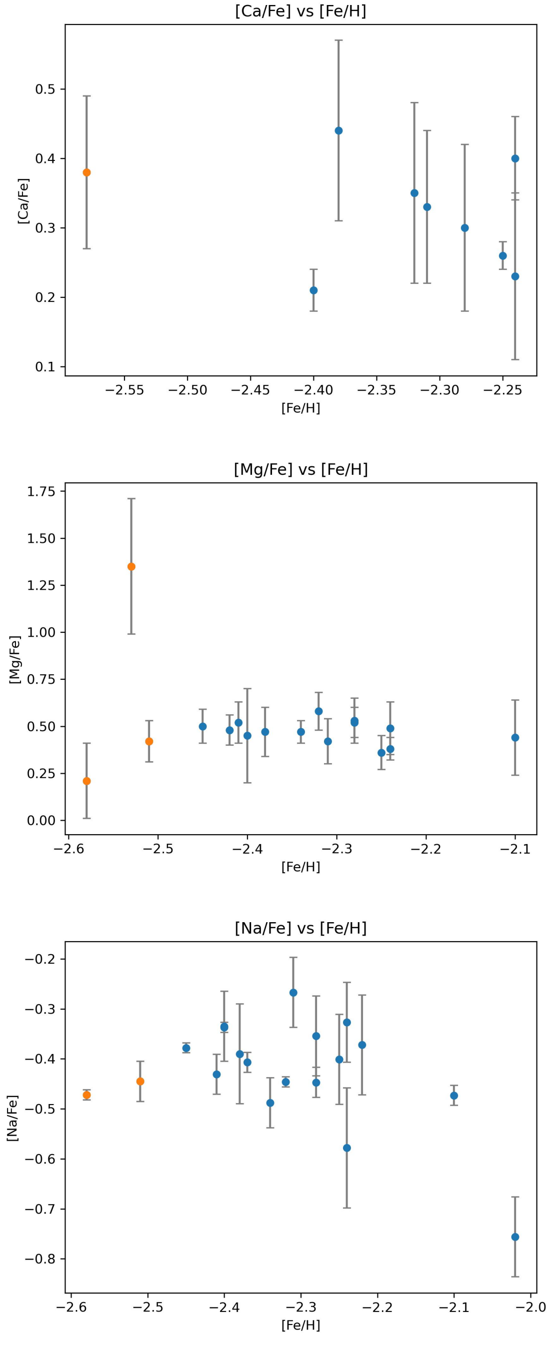

Figure 5.10: In this plot the results regarding the abundances of Ca (on the left), Mg (in the centre) and Na (on the right) as a function of [Fe/H] are reported. In blue we have the result for stars fitted by the isochrone, while in orange we have the result for the stars falling outside of the isochrone.

Here both the values obtained for the abundances of lighter elements and the corresponding errors are represented. Concerning Na and Mg, we studied their intrinsic scatter in order to highlight possible intrinsic spread compatible with those observed in globular clusters. We can notice that there is not a significant scatter in the abundances of such elements. As a further check of this result we have made, for the Na abundances, a plot providing a comparison between the result found by Carretta et al., 2009 for galactic globular clusters with [Fe/H]$\in [-2.5, -2.0]$ dex, similar to the value found for ED-2, and our work (see Fig.5.11). We noticed that ED-2 has a very small spread with respect to the one characterising other galactic globular clusters with similar [Fe/H]. This may be due to our low statistics or it could be a sign of the absence of such spread. To understand better which is our case, we have run once again the MCMC code (the same used for the determination of the intrinsic spread of the MDF) on the Na abundances obtained in this work (see Tab.5.3). The MCMC gives an intrinsic scatter for Na of 0.06±0.02, which means that the intrinsic spread is null at almost 3σ. This is a rather borderline case because such spread is not typical of a cluster.

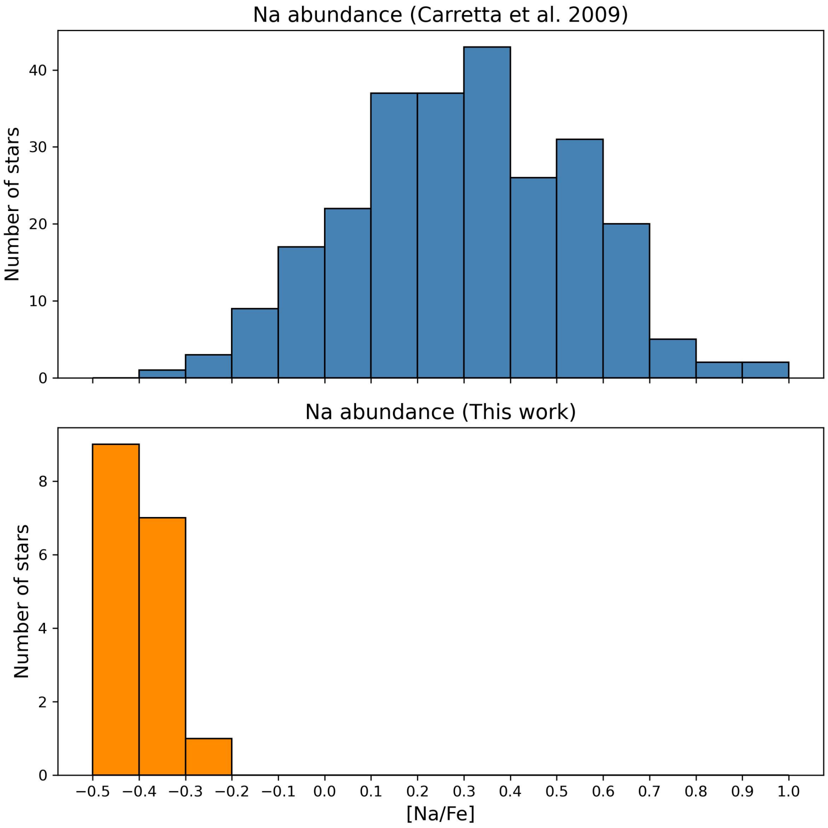

Figure 5.11: *Top panel*: distribution representing the Na abundances in galactic clusters analysed by Carretta et al., 2009. *Bottom panel*: distribution representing the Na abundances in ED-2.

Knowing that the presence of the anti-correlations is actually what would clarify the nature of ED-2's progenitor though, the absence of the scatter is not necessarily implying any conclusive result for which we would need at least C, N, O and Al lines that are not visible in our spectra. Specifically, the reason why such lines haven't been detected is that the strongest lines that we could use are in the blue part of the spectra, but this spectral range is here characterised by a very low signal to noise ratio that doesn't allow us to analyse these features and hence to see possible anti-correlations.

name	[Na/Fe] (dex)
star2	-0.33±0.08
star3	-0.47±0.04
star4	-0.58±0.12
star5	-0.40±0.09
star6	-0.27±0.07
star7	-0.35±0.08
star8	-0.37±0.10
star10	-0.34±0.07
star11	-0.39±0.10
star13	-0.45±0.04
star14	-0.43±0.04
star16	-0.38±0.04
star17	-0.49±0.05
star18	-0.47±0.02
star20	-0.34±0.04
star21	-0.45±0.04
star22	-0.76±0.08
star23	-0.45±0.03
star24	-0.41±0.02

Table 5.3: Measures for the [Na/Fe] abundance obtained from our sample.

name	[Mg/Fe] (dex)
star2	0.38±0.06
star3	0.21±0.20
star4	0.49±0.14
star5	0.36±0.09
star6	0.42±0.12
star7	0.52±0.08
star9	0.58±0.10
star10	0.45±0.25
star11	0.47±0.13
star12	0.48±0.08
star13	0.42±0.11
star14	0.52±0.11
star15	1.35±0.36
star16	0.50±0.09
star17	0.47±0.06
star18	0.44±0.20
star23	0.53±0.12

Table 5.4: Measures for the [Mg/Fe] abundance obtained from our sample.

name	[Ca/Fe] (dex)
star2	0.40±0.06
star3	0.38±0.11
star4	0.23±0.12
star5	0.26±0.02
star6	0.33±0.11
star7	0.30±0.12
star9	0.35±0.13
star10	0.21±0.03
star11	0.44±0.13

Table 5.5: Measures for the [Ca/Fe] abundance obtained from our sample.

Chapter 6

Conclusions

The ED-2 system represents one of the most intriguing dynamical substructures recently identified in the solar neighbourhood. As reported by Dodd et al., 2023, ED-2 stands out due to its compactness in velocity space, indicating that it has not yet undergone full phase mixing and that its stars are still coherently moving through the Milky Way's disc. The photometric analysis by Balbinot et al., 2023 further revealed that both the main sequence and the red giant branch are consistent with a single, very old stellar population with an age of log(age/yr) = 10.20, raising questions about the true nature of ED-2's progenitor.

The analysis of the MDF presented in this work provided an accurate estimate of the system's mean metallicity and intrinsic dispersion. Using the MCMC approach described in Chapter 5, we derived a mean value of [Fe/H] = -2.33 ± 0.03 dex with an intrinsic scatter of 0.13±0.02 dex, adopting the entire sample of stars with measurable [Fe/H]. When we exclude 2 stars whose position in the CMD is not compatible with a single-age population (at variance with all the other targets), the MCMC approach provides[Fe/H]= -2.33 ± 0.01 dex, which is in excellent agreement with previous studies and, most importantly, shows an intrinsic scatter consistent with zero.
This indicates that the observed spread in [Fe/H] can be fully explained by measurement uncertainties rather than by a true variation in iron abundance among the stars. Such evidence strongly supports the scenario in which ED-2 originated as one of the most metal-poor globular clusters accreted onto the Milky Way halo, in agreement with the findings of Balbinot et al., 2023, Ceccarelli et al., 2024, and Dodd et al., 2025.

Also, we analysed both the abundances of light elements (Mg and Na), which are key tracers for investigating the presence of chemical anti-correlations, a hallmark of multiple stellar populations in globular clusters, and Ca which is a tracer of the chemical enrichment by different kind of SNe. The results show no significant scatter in these abundances; however, the absence of an evident anti-correlation is not conclusive. Indeed, diagnostic lines for crucial elements such as C, N, O, and Al, which are essential for confirming or excluding such patterns, lie in the blue spectral range, where the current spectra suffer from low signal-to-noise ratios, preventing a reliable measurement. For this reason, an essential future step will be the acquisition of high-quality data in the blue wavelength range (an observing proposal with X-SHOOTER@VLT has been submitted at ESO for the period 117 with this aim, PI:Covella). These new observations will allow us to measure the abundances of carbon, nitrogen, and aluminium and to search for possible C–N and Mg–Al anti-correlations. Detecting such abundance patterns would provide definitive proof that ED-2 is a globular cluster, making it the most metal-poor one known in the Milky Way. Conversely, the absence of such correlations would support the alternative scenario in which ED-2 originated from a disrupted dwarf galaxy.

In conclusion, the results of this thesis provide strong evidence supporting the hypothesis that ED-2 is the remnant of a dissolved, metal-poor globular cluster accreted onto the Galactic halo. Nevertheless, further analysis of other light-element abundances (i.e. C, N, Al) is crucial to conclusively confirm its nature. Understanding ED-2's origin not only sheds light on the evolution of this individual system but also contributes to reconstructing the hierarchical assembly history of the Milky Way halo, offering a unique glimpse into the earliest stages of our Galaxy's formation.

Bibliography

Andrae, R., Fouesneau, M., Creevey, O., Ordenovic, C., Mary, N., Burlacu, A., Chaoul, L., Jean-Antoine-Piccolo, A., Kordopatis, G., Korn, A., Lebreton, Y., Panem, C., Pichon, B., Thévenin, F., Walmsley, G., & Bailer-Jones, C. A. L. (2018). Gaia Data Release 2. First stellar parameters from Apsis., *616*, Article A8, A8. https://doi.org/10.1051/0004-6361/201732516

Balbinot, E., Helmi, A., Callingham, T., Matsuno, T., Dodd, E., & Ruiz-Lara, T. (2023). Ed-2: A cold but not so narrow stellar stream crossing the solar neighbourhood. *Astronomy amp; Astrophysics*, *678*, A115. https://doi.org/10.1051/0004-6361/202347076

Bastian, N., & Lardo, C. (2018). Multiple Stellar Populations in Globular Clusters., *56*, 83–136. https://doi.org/10.1146/annurev-astro-081817-051839

Belokurov, V., Erkal, D., Evans, N. W., Koposov, S. E., & Deason, A. J. (2018). Co-formation of the disc and the stellar halo. *Monthly Notices of the Royal Astronomical Society*, *478*(1), 611–619. https://doi.org/10.1093/mnras/sty982

Belokurov, V., & Kravtsov, A. (2022). From dawn till disc: Milky way's turbulent youth revealed by the apogee+gaia data. *Monthly Notices of the Royal Astronomical Society*, *514*(1), 689–714. https://doi.org/10.1093/mnras/stac1267

Boeltzig, A., Bruno, C. G., Cavanna, F., Cristallo, S., Davinson, T., Depalo, R., deBoer, R. J., Di Leva, A., Ferraro, F., Imbriani, G., Marigo, P., Terrasi, F., & Wiescher, M. (2016). Shell and explosive hydrogen burning. Nuclear reaction rates for hydrogen burning in RGB, AGB and Novae. *European Physical Journal A*, *52*(4), Article 75, 75. https://doi.org/10.1140/epja/i2016-16075-4

Brown, A. G. A., Vallenari, A., Prusti, T., de Bruijne, J. H. J., Babusiaux, C., Bailer-Jones, C. A. L., Biermann, M., Evans, D. W., Eyer, L., Jansen, F., Jordi, C., Klioner, S. A., Lammers, U., Lindegren, L., Luri, X., Mignard, F., Panem, C., Pourbaix, D., Randich, S., … Zwitter, T. (2018). Gaia data release 2: Summary of the contents and survey properties. *Astronomy amp; Astrophysics*, *616*, A1. https://doi.org/10.1051/0004-6361/201833051

Carretta, E., Bragaglia, A., Gratton, R., & Lucatello, S. (2009). Na-O anticorrelation and HB. VIII. Proton-capture elements and metallicities in 17 globular clusters from UVES spectra., *505*(1), 139–155. https://doi.org/10.1051/0004-6361/200912097

Castelli, F., & Kurucz, R. L. (2003, January). New Grids of ATLAS9 Model Atmospheres. In N. Piskunov, W. W. Weiss, & D. F. Gray (Eds.), *Modelling of stellar atmospheres* (A20, Vol. 210). https://doi.org/10.48550/arXiv.astro-ph/0405087

Ceccarelli, E., Massari, D., Mucciarelli, A., Bellazzini, M., Nunnari, A., Cusano, F., Lardo, C., Romano, D., Ilyin, I., & Stokholm, A. (2024). A walk on the retrograde side (wrs) project. i. tidying-up the retrograde halo with high-resolution spectroscopy. https://arxiv.org/abs/2401.04184

Dekker, H., D'Odorico, S., Kaufer, A., Delabre, B., & Kotzlowski, H. (2000). Design, construction, and performance of UVES, the echelle spectrograph for the UT2 Kueyen Telescope at the ESO Paranal Observatory. In M. Iye & A. F. M. Moorwood (Eds.), *Optical and ir telescope instrumentation and detectors* (pp. 534–545, Vol. 4008). SPIE. https://doi.org/10.1117/12.395512

Dodd, E., Callingham, T. M., Helmi, A., Matsuno, T., Ruiz-Lara, T., Balbinot, E., & Lövdal, S. (2023). Gaia dr3 view of dynamical substructure in the stellar halo near the sun. *Astronomy amp; Astrophysics*, *670*, L2. https://doi.org/10.1051/0004-6361/202244546

Dodd, E., Matsuno, T., Helmi, A., Balbinot, E., Callingham, T. M., Starkenburg, E., Woudenberg, H. C., & Ruiz-Lara, T. (2025). Chemical characterisation of small substructures in the local stellar halo. *Astronomy amp; Astrophysics*. https://doi.org/10.1051/0004-6361/202554252

ESA Gaia Archive. (2025). Gaia archive — european space agency [Accessed: October 2025].

ESA Gaia Collaboration. (2021). Gaia edr3 extinction laws [Accessed: October 2025].

EXPLORE Consortium. (2021). Explore platform: Innovative scientific data exploration and exploitation for space science [European Union Horizon 2020 project, Grant Agreement No. 101004214].

Fernández-Alvar, E., Ruiz-Lara, T., Gallart, C., Cassisi, S., Surot, F., González-Koda, Y. K., Callingham, T. M., Queiroz, A. B., Battaglia, G., Thomas, G., Chiappini, C., Hill, V., Dodd, E., Helmi, A., Aznar-Menargues, G., de la Cueva, A., Mirabla, D., Quintana-Ansaldo, M., & Rivero, A. (2025). Chronology of our galaxy from gaia colour-magnitude diagram fitting (chronogal) ii. unveiling the formation and evolution of the kinematically selected thick and thin discs. https://arxiv.org/abs/2503.19536

Gaia Collaboration, Prusti, T., de Bruijne, J. H. J., Brown, A. G. A., Vallenari, A., Babusiaux, C., Bailer-Jones, C. A. L., Bastian, U., Biermann, M., Evans, D. W., Eyer, L., Jansen, F., Jordi, C., Klioner, S. A., Lammers, U., Lindegren, L., Luri, X., Mignard, F., Milligan, D. J., … Zschocke, S. (2016). The gaia mission. *AA*, *595*, A1. https://doi.org/10.1051/0004-6361/201629272

Gaia Collaboration, Vallenari, A., Brown, A. G. A., Prusti, T., de Bruijne, J. H. J., Arenou, F., Babusiaux, C., Biermann, M., Creevey, O. L., Ducourant, C., Evans, D. W., Eyer, L., Guerra, R., Hutton, A., Jordi, C., Klioner, S. A., Lammers, U. L., Lindegren, L., Luri, X., … De March, R. (2023). Gaia Data Release 3. Summary of the content and survey properties., *674*, Article A1, A1. https://doi.org/10.1051/0004-6361/202243940

Gallart, C., Bernard, E. J., Brook, C. B., Ruiz-Lara, T., Cassisi, S., Hill, V., & Monelli, M. (2019). Uncovering the birth of the milky way through accurate stellar ages with gaia. *Nature Astronomy*, *3*(10), 932–939. https://doi.org/10.1038/s41550-019-0829-5

Gratton, R., Sneden, C., & Carretta, E. (2004). Abundance Variations Within Globular Clusters., *42*(1), 385–440. https://doi.org/10.1146/annurev.astro.42.053102.133945

Helmi, A. (2020). Streams, substructures, and the early history of the milky way. *Annual Review of Astronomy and Astrophysics*, *58*(1), 205–256. https://doi.org/10.1146/annurev-astro-032620-021917

Helmi, A., Babusiaux, C., Koppelman, H. H., Massari, D., Veljanoski, J., & Brown, A. G. A. (2018). The merger that led to the formation of the milky way's inner stellar halo and thick disk. *Nature*, *563*(7729), 85–88. https://doi.org/10.1038/s41586-018-0625-x

Helmi, A., & de Zeeuw, P. T. (2000). Mapping the substructure in the Galactic halo with the next generation of astrometric satellites., *319*(3), 657–665. https://doi.org/10.1046/j.1365-8711.2000.03895.x

Helmi, A., White, S. D. M., de Zeeuw, P. T., & Zhao, H. (1999). Debris streams in the solar neighbourhood as relicts from the formation of the milky way. *Nature*, *402*(6757), 53–55. https://doi.org/10.1038/46980

Koppelman, H., Helmi, A., & Veljanoski, J. (2018). One large blob and many streams frosting the nearby stellar halo in gaia dr2. *The Astrophysical Journal Letters*, *860*(1), L11. https://doi.org/10.3847/2041-8213/aac882

Koppelman, H. H., Bos, R. O. Y., & Helmi, A. (2020). The messy merger of a large satellite and a milky way-like galaxy. *Astronomy amp; Astrophysics*, *642*, L18. https://doi.org/10.1051/0004-6361/202038652

Koppelman, H. H., Helmi, A., Massari, D., Price-Whelan, A. M., & Starkenburg, T. K. (2019). Multiple retrograde substructures in the galactic halo: A shattered view of galactic history. *Astronomy amp; Astrophysics*, *631*, L9. https://doi.org/10.1051/0004-6361/201936738

Kurucz, R. L. (1993). Synthe spectrum synthesis programs and line data [Includes WIDTH9 code. Available at http://kurucz.harvard.edu/programs/WIDTH/].

Lane, J., Bovy, J., & Mackereth, T. (2023). The stellar mass of the gaia-sausage/enceladus accretion remnant. https://arxiv.org/abs/2306.03084

Lindegren, L., Bastian, U., Biermann, M., Bombrun, A., de Torres, A., Gerlach, E., Geyer, R., Hernández, J., Hilger, T., Hobbs, D., Klioner, S. A., Lammers, U., McMillan, P. J., Ramos-Lerate, M., Steidelmüller, H., Stephenson, C. A., & van Leeuwen, F. (2021). Gaia Early Data Release 3. Parallax bias versus magnitude, colour, and position., *649*, Article A4, A4. https://doi.org/10.1051/0004-6361/202039653

Luo, A.-L., Zhao, Y.-H., Zhao, G., Deng, L.-C., Liu, X.-W., Jing, Y.-P., Wang, G., Zhang, H.-T., Shi, J.-R., Cui, X.-Q., Chu, Y.-Q., Li, G.-P., Bai, Z.-R., Wu, Y., Cai, Y., Cao, S.-Y., Cao, Z.-H., Carlin, J. L., Chen, H.-Y., … Zuo, F. (2015). The first data release (dr1) of the lamost regular survey. *Research in Astronomy and Astrophysics*, *15*(8), 1095–1124. https://doi.org/10.1088/1674-4527/15/8/002

Majewski, S. R., Schiavon, R. P., Frinchaboy, P. M., Allende Prieto, C., Barkhouser, R., Bizyaev, D., Blank, B., Brunner, S., Burton, A., Carrera, R., Chojnowski, S. D., Cunha, K., Epstein, C., Fitzgerald, G., García Pérez, A. E., Hearty, F. R., Henderson, C., Holtzman, J. A., Johnson,

J. A., … Zamora, O. (2017). The Apache Point Observatory Galactic Evolution Experiment (APOGEE)., *154*(3), Article 94, 94. https://doi.org/10.3847/1538-3881/aa784d

Matsuno, T., Dodd, E., Koppelman, H. H., Helmi, A., Ishigaki, M. N., Aoki, W., Zhao, J., Yuan, Z., & Hattori, K. (2022). High-precision chemical abundances of galactic building blocks: Ii. revisiting the chemical distinctness of the helmi streams. *Astronomy amp; Astrophysics*, *665*, A46. https://doi.org/10.1051/0004-6361/202243609

Matteucci, F., & Romano, D. (1999). The Chemical Evolution of the Galactic Bulge., *265*, 311–318. https://doi.org/10.1023/A:1002172113229

McLaughlin, D. E., & van der Marel, R. P. (2005). Resolved Massive Star Clusters in the Milky Way and Its Satellites: Brightness Profiles and a Catalog of Fundamental Parameters., *161*(2), 304–360. https://doi.org/10.1086/497429

Mucciarelli, A. (2013). 4dao cookbook. https://arxiv.org/abs/1311.1403

Mucciarelli, A., Bellazzini, M., & Massari, D. (2021). Exploiting the Gaia EDR3 photometry to derive stellar temperatures., *653*, Article A90, A90. https://doi.org/10.1051/0004-6361/202140979

Mucciarelli, A., Pancino, E., Lovisi, L., Ferraro, F. R., & Lapenna, E. (2013). GALA: An Automatic Tool for the Abundance Analysis of Stellar Spectra., *766*(2), Article 78, 78. https://doi.org/10.1088/0004-637X/766/2/78

Myeong, G. C., Vasiliev, E., Iorio, G., Evans, N. W., & Belokurov, V. (2019). Evidence for two early accretion events that built the milky way stellar halo. *Monthly Notices of the Royal Astronomical Society*, *488*(1), 1235–1247. https://doi.org/10.1093/mnras/stz1770

Oria, P.-A., Tenachi, W., Ibata, R., Famaey, B., Yuan, Z., Arentsen, A., Martin, N., & Viswanathan, A. (2022). Antaeus: A retrograde group of tidal debris in the milky way's disk plane. *The Astrophysical Journal Letters*, *936*(1), L3. https://doi.org/10.3847/2041-8213/ac86d3

Pietrinferni, A., Hidalgo, S., Cassisi, S., Salaris, M., Savino, A., Mucciarelli, A., Verma, K., Silva Aguirre, V., Aparicio, A., & Ferguson, J. W. (2021). Updated BaSTI Stellar Evolution Models and Isochrones. II. α-enhanced Calculations., *908*(1), Article 102, 102. https://doi.org/10.3847/1538-4357/abd4d5

Ruiz-Lara, T., Matsuno, T., Lövdal, S. S., Helmi, A., Dodd, E., & Koppelman, H. H. (2022). Substructure in the stellar halo near the sun: Ii. characterisation of independent structures. *Astronomy amp; Astrophysics*, *665*, A58. https://doi.org/10.1051/0004-6361/202243061

Stetson, P. B., & Pancino, E. (2008). DAOSPEC: An Automatic Code for Measuring Equivalent Widths in High-Resolution Stellar Spectra., *120*(874), 1332. https://doi.org/10.1086/596126

Strassmeier, K. G., Ilyin, I., Järvinen, A., Weber, M., Woche, M., Barnes, S. I., Bauer, S. .-., Beckert, E., Bittner, W., Bredthauer, R., Carroll, T. A., Denker, C., Dionies, F., DiVarano, I., Döscher, D., Fechner, T., Feuerstein, D., Granzer, T., Hahn, T., … Sablowski, D. (2015). PEPSI: The high-resolution échelle spectrograph and polarimeter for the Large Binocular Telescope. *Astronomische Nachrichten*, *336*(4), 324. https://doi.org/10.1002/asna.201512172

Tolstoy, E., Hill, V., & Tosi, M. (2009). Star-formation histories, abundances, and kinematics of dwarf galaxies in the local group. *Annual Review of Astronomy and Astrophysics*, *47*(1), 371–425. https://doi.org/10.1146/annurev-astro-082708-101650

Tonry, J., & Davis, M. (1979). A survey of galaxy redshifts. I. Data reduction techniques., *84*, 1511–1525. https://doi.org/10.1086/112569

Vasiliev, E., & Belokurov, V. (2020). The last breath of the sagittarius dsph. *Monthly Notices of the Royal Astronomical Society*, *497*(4), 4162–4182. https://doi.org/10.1093/mnras/staa2114

Zwitter, T., Kos, J., Chiavassa, A., Buder, S., Traven, G., Čotar, K., Lin, J., Asplund, M., Bland-Hawthorn, J., Casey, A. R., De Silva, G., Duong, L., Freeman, K. C., Lind, K., Martell, S., D'Orazi, V., Schlesinger, K. J., Simpson, J. D., Sharma, S., … Žerjal, M. (2018). The galah survey: Accurate radial velocities and library of observed stellar template spectra. *Monthly Notices of the Royal Astronomical Society*, *481*(1), 645–654. https://doi.org/10.1093/mnras/sty2293